LBNL-45257

Ga Self-Diffusion in Isotopically Enriched GaAs Heterostructures Doped with Si and Zn

Marshall Stephen Norseng

Materials Sciences Division
Ernest Orlando Lawrence Berkeley National Laboratory
1 Cyclotron Road
Berkeley, California 94720

and

Department of Materials Science and Mineral Engineering
University of California
Berkeley, California 94720

M.S. Thesis

December 1999

This work was supported by the Director, Office of Science, Office of Basic Energy Sciences, Division of Materials Sciences, of the U.S. Department of Energy under Contract No. DE-AC03-76SF00098 and by U.S. NSF grant DMR-97 32707.

DISCLAIMER

Ga Self-Diffusion in Isotopically Enriched GaAs Heterostructures Doped with Si and Zn

by

Marshall Stephen Norseng

B.S. (University of Wisconsin at Madison) 1997

A thesis submitted in partial satisfaction of the

requirements for the degree of

Masters of Science

in

Engineering – Materials Science and Mineral Engineering

in the

GRADUATE DIVISION

of the

UNIVERSITY of CALIFORNIA at BERKELEY

Committee in Charge:

Prof. Eugene E. Haller, Chair
Prof. Timothy D. Sands
Prof. Paul Wright

Fall 1999

Acknowledgements

There are many people whose help and support made this thesis possible. First, I would like to earnestly thank Prof. Haller for his straightforward explanations and advising, research feedback, and financial support. I greatly appreciate Prof. Sands and Prof. Wright for their enthusiastic classroom instruction and serving on my thesis committee. A special thanks goes to Dr. Hartmut Bracht without whom this work would not have been as complete or timely. During his yearlong stay at Lawrence Berkeley National Lab and subsequent return to Germany, Dr. Bracht provided invaluable insight into the experimental techniques used in this study and provided the numerical simulations to model the diffusion experiments. Techniques and explanations that were new to me but that I'm certain he had repeated many times before were always delivered with enthusiasm, an emphasis on precision, as well as good humor. I would also like to thank the students of the Haller group for their camaraderie and assistance, especially Raechelle Wong and Hughes Silvestri. Jeff Beeman made experiments much more precise and efficient with the generous use of his equipment and troubleshooting expertise, Dr. Edith Bourret donated GaAs wafers for use as sample substrates for test runs, and David Hom helped direct me through the LBL purchasing and HR hoops with ease and irreverent sarcasm. Finally I thank my family for their moral support and especially Aimee for understanding when ampoules put me in a bad mood and most of all for making the last two years as balanced as graduate school would allow.

This work was supported by U.S. NSF grant DMR-97 32707 and by the Director, Office of Science, Office of Basic Energy Sciences, Division of Materials Sciences of the U.S. Department of Energy under contract No.DE-AC03-76SF00098.

Table of Contents

1. Introduction

The tremendous advances in semiconductor process and device technology over the last few decades have been much chronicled, and such reviews usually focus on the commercial success of silicon based solid state integrated circuits. While it is undisputed that Si is commercially the most utilized semiconductor, GaAs and related compound semiconductors have been the standard materials for optoelectronic devices such as light emitting diodes and lasers, high electron mobility transistors (HEMTs) and hold the promise of allowing integrated circuits which operate using photons in addition to electrons and holes. Among the advantages of GaAs based materials for such advanced devices is a direct band gap allowing single event emission and absorption of photons, the possibility to create layered structures with varying band gaps and alloy composition, and band gap energies covering the full spectrum of visible light.

Any success in materials must be accompanied by process development and, in turn, successful process development requires knowledge of basic material properties such as how a material can be deposited, etched, implanted with impurities and how these impurities diffuse. Nearly 20 years ago researchers at the University of Illinois reported some unusual diffusion behavior in superlattices comprised of two of the most commonly layered III-V materials, AlAs and GaAs. Specifically, AlAs/GaAs layers diffused with Zinc converted into a homogenous AlGaAs alloy at a temperature that causes imperceptible distortion of the same layered structures when the Zinc was excluded from the process. This disordering process could be of benefit to device processing since controlled use of this impurity induced layer disordering (IILD) could provide a low cost method of isolating integrated optically active structures. Obviously, IILD could also be

very detrimental to device processing but the behavior has yet to be accurately modeled due to difficulties monitoring, deconvolving, and modeling the movement of both the native defects and impurity species present in the III-V system.

This study attempts to advance the modeling of AlGaAs/GaAs/AlAs diffusion by experimental investigation of Ga self-diffusion in undoped, as-grown doped and Zinc diffused structures. We utilize novel, isotopically enriched superlattice and heterostructure samples to provide direct observation and accurate measurement of diffusion with a precision not possible using conventional techniques.

Please note that for readability, except for where explicitly stated otherwise, the term semiconductor(s) implies single crystal semiconductor(s), the term AlGaAs refers to a range of $Al_xGa_{1-x}As$ compounds, and the term III-V semiconductors refers to the range of stable compounds consisting of Al, Ga, or In as the cation and N, P, As or Sb as the anion.

1.1. Key Physical Properties of AlGaAs

A set of physical properties originating in the band structure of several III-V semiconductors make this family of materials particularly appealing for advanced electro-optical or rapidly switching devices.

First, we consider the direct band gap of many group III-V materials, which unlike conventional silicon allows for the direct generation or absorption of photons from a single electron (hole) transition. The valence and conduction band extrema occur at the same point in the Brillouin zone (at k=0) and are separated by an energy of 1.43 eV in GaAs. In contrast, the transition across the minimum energy band separation in Si

requires 1.11eV of energy and occurs at different k values in the Brillouin zone [figure 1-1]. For direct band gap materials, electrons can make transitions directly between energy bands accompanied by the emission or absorption of a single photon. No change in momentum is needed to make the transition. Conversely, indirect band gap materials require a deep level state within the band gap, phonon interaction or some other mechanism to conserve momentum and energy for the recombination of electrons and holes at the band extrema. Applied to devices this means that photons can be generated or absorbed much more efficiently in direct band gap materials than in indirect materials. Also, because of the more efficient absorption of light, the photon penetration depth is much shorter in GaAs. This means that GaAs devices can absorb the same number of photon in layers 10-100x thinner than Si making the required dimensions for devices much smaller.

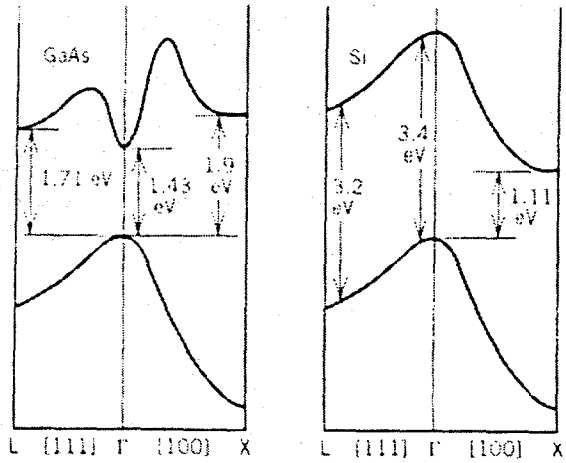

Figure 1-1: The direct band structure of GaAs showing the valence band maximum and conduction band minimum at the same wave vector with a separation of 1.43eV. For Si the minimum band separation occurs for band extrema at different k values. (Ghandi 1994)

Second, electrons in GaAs have a lower effective mass than in silicon. The effective mass of an electron is inversely proportional to the curvature of the conduction band at its minimum. The low effective electron mass of GaAs translates into high electron mobility

resulting in high-speed operation of n-type devices and low voltage requirements because the 'lighter' electrons have a high drift velocity at moderate electric fields. Also, III-V semiconductor materials cover a wide range of band gaps allowing 'band gap engineering' to tailor photon absorption (generation) or heterostructure band offset to specific energies. Alloy compositions between binary compounds have lattice parameters and band gaps that cover the range of values between the two component alloys, though not necessarily in a linear manner. Figure 1-2 shows the lattice constant and band gap of many III-V semiconductor alloys along with some other semiconductors of interest. Finally, AlGaAs and many other III-V materials have a band gap larger than silicon. This

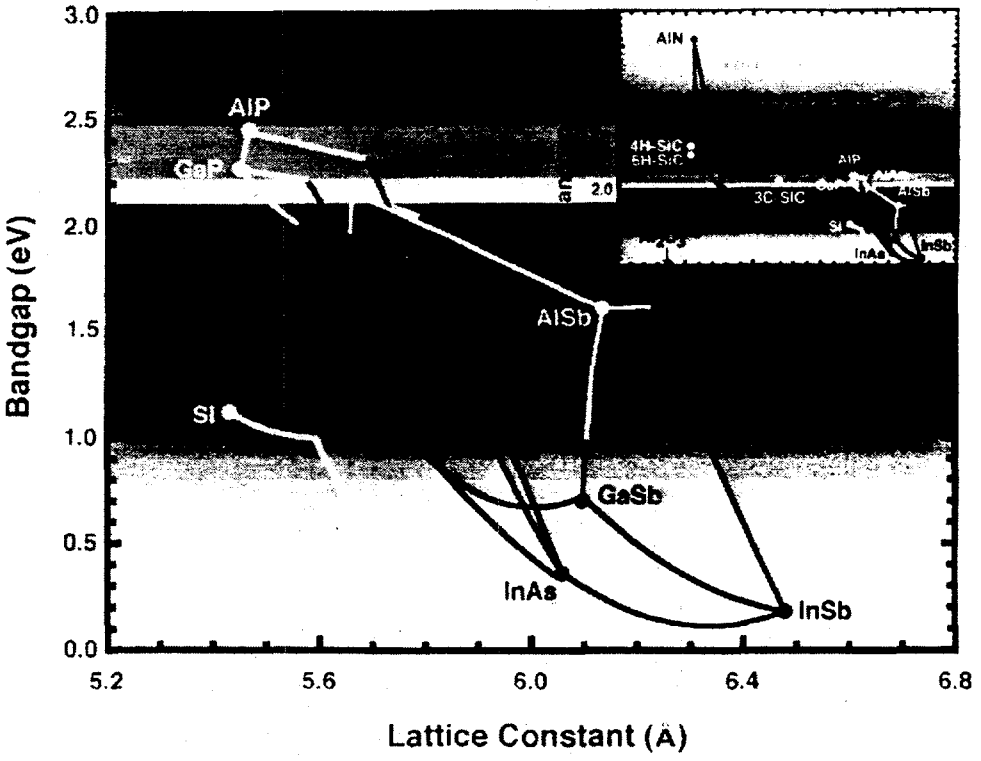

Figure 1-2: The lattice parameter vs. band gap for III-V semiconductors. Direct band gap materials are shown in black and indirect materials in gray. (MellWood Laboratories)

larger energy gap leads to a lower intrinsic carrier concentration at a given temperature so that doped materials (devices) remain extrinsic (functional) to temperatures higher than in Si.

1.2. Crystal Structure and Point Defects

Atoms in GaAs and AlAs form a Zincblende structure that consists of a Ga/Al f.c.c lattice interlocked with an As f.c.c lattice. The conjugate unit cell has one species at the cell corners (1,0,0; 0,1,0; etc.) and face centers (½, ½, 0; ½, 0, ½; etc.) and the other species are located at alternate interstices of the cell (¼, ¼, ¼; ¾, ¼, ¼; etc) [figure 1-3]. Using a hard sphere model, a lattice parameter of 5.65Å and atomic radii of 1.18Å and 1.26Å for As and Ga, a GaAs unit cell leaves 66% of the space unoccupied. The space in an AlAs crystal is nearly 70% unoccupied. Thus the zinc blend lattice is a very open structure leaving much space for interstitial diffusion. AlAs and GaAs based alloys of different compositions are often used in multilayer structures because they not only share the same crystal structure but the lattice constants of the two materials are nearly identical.

The lattice constant of stoichiometric, undoped GaAs is 5.65325Å compared to 5.6607Å for AlAs with the lattice constant of intermediary $Al_{1-x}Ga_xAs$ alloys scaling linearly with x between the binary alloy values. With a maximum of 0.13% lattice mismatch, epitaxial growth of a film of one compound on the nearly identical crystal template of the other is generally straightforward.

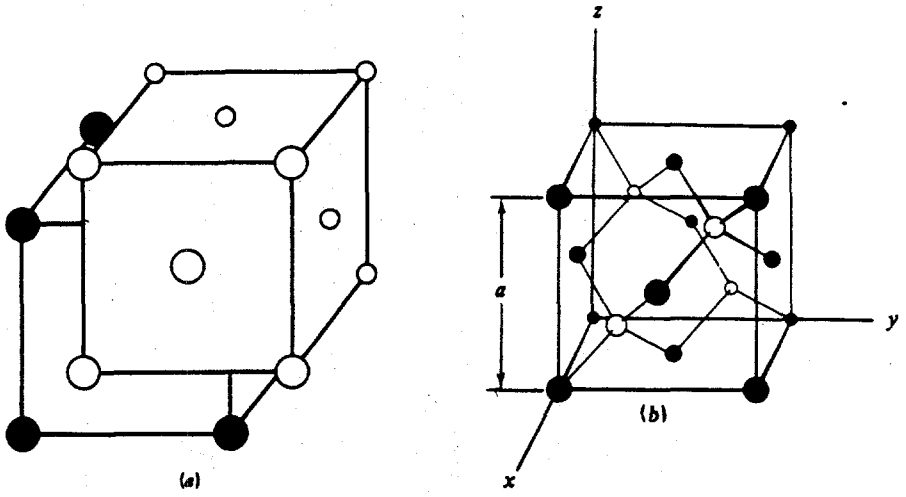

Figure 1-3: Overlapping face centered cubic (f.c.c.) lattices of Ga atoms (solid circles) and As atoms (empty circles) (a) jointly form the GaAs zincblende lattice (b) (Ghandi 1994)

Perfect bulk crystals are thermodynamically not possible. The addition of defects to crystal lattices increases the entropy, which in turn reduces the total energy of the system. The localized (point) defects that are always presents in crystal influence the electronic properties of the material and are the conduits of all self-diffusion. In pure GaAs there are four general types of point defects possible in the lattice: Ga and As vacancies, Ga and As in an interstitial opening of the lattice, Ga on an As site or vice versa, as well as paired combinations of the three general types. The equilibrium concentration of a given point defect is solely related to its formation energy and the temperature of the system. For example the equilibrium vacancy concentration [v] is given by

$$[\mathrm{v}] = Ne^{-\frac{E_v}{T}} \tag{1.1}$$

Where E_v is the formation energy of the vacancy, N is the number of occupied lattice sites, and T is the absolute temperature of the system. The equilibrium concentrations of interstitials and anitsite defects are given by similar expressions.

Equation 1.1 applies only to defects that are neutral. In GaAs and other semiconductor materials it is known that many point defects carry an electric charge and their concentration is thus influenced by the position of the Fermi level. For example, the energy required for the formation of a doubly negatively charged Ga vacancy, V_{Ga}^{2-}, depends on the energy difference between the V_{Ga}^{2-} energy level and the Fermi level since the transition of -2q charge from the Fermi level to the lower energy level of the vacancy reduces the total formation energy of the defect. As seen in figure 1-4, in highly doped

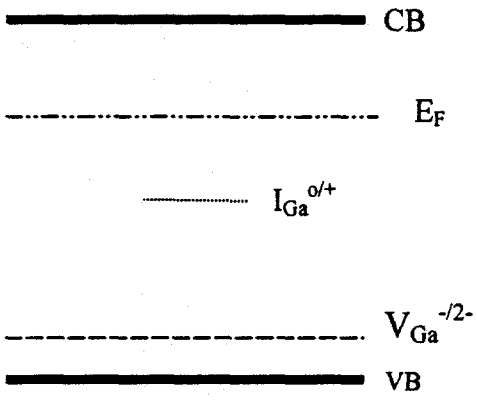

Figure 1-4:Examples of defect energy levels in a semiconductor

n-type material, with the V_{Ga}^{2-} level near the valence band, there is a reduction in the defect formation energy by twice the electron transition energy. Conversely, positively charged defects, such as I_{Ga}^{2+} will increase in concentration as the Fermi level approaches the valence band. The concentration of vacancies (or other defects) in a crystal is described by the sum of the neutral defect (which is independent of the Fermi level) and

all the charged variations of the same defect. Hence, the total defect concentration is strongly influenced by the position of the Fermi level in the material.

While the concentration of point defects in some material systems depends mainly on the temperature, the exterior partial pressures of the two components forming the crystal lattice play a dominant role in determining the defect concentrations in GaAs. Incongruent surface evaporation occurs at temperatures below the melting temperature and can result in the disproportionate loss of the more volatile component, As. The reaction given in equation 1.2 describes congruent decomposition at a temperature where As_4 is the most stable As product.

$$GaAs(s) \Leftrightarrow Ga(g) + \frac{1}{4} As_4(g) \tag{1.2}$$

This leads to a corresponding mass action relationship given in equation1.2a where p_x is the partial pressure of the elements in gaseous form.

$$p_{Ga} = k_2 p_{As_4}^{-1/4} \tag{1.2a}$$

The evaporation of one lattice component causes vacancies in the crystal, the concentration of which can be related back to the partial pressures of the constituents in the system by mass action relationships. In the reaction above for each Ga vacancy created by evaporation four As atoms evaporate and thus the Ga vacancy concentration is proportional to $p_{As_4}^{-1/4}$. In actuality vacancies on the Ga sublattice are believed to exist in the V^-, V^{2-} or V^{3-} configurations (Cohen 1997; Yu, et al. 1991) . Formation of these defects occurs via the reactions and mass action relationships given in equations 1.3 and 1.4, where p is the hole concentration in the material.

$$Ga(s) \Leftrightarrow V_{Ga}^- + Ga(g) + h^+ \tag{1.3}$$

$$\left[V_{Ga}^{2-}\right]p = k_3 p_{Ga}^{-1} \tag{1.3b}$$

$$Ga(s) \Leftrightarrow V_{Ga}^{2-} + Ga(g) + 2h^{+} \tag{1.4}$$

$$\left[V_{Ga}^{-}\right]p = k_4 p_{Ga}^{-2} \tag{1.4b}$$

Combining these equations with the intrinsic carrier concentration relationship for a semiconductor, $n_i^2 = np$, the concentration of Ga individual vacancy species depend on the As partial pressure and carrier concentration of the material, equations 1.5 and 1.6.

$$[V_{Ga}^{-}] = k_5 \frac{n}{n_i^2} p_{As_4}^{1/4} \tag{1.5}$$

$$[V_{Ga}^{2-}] = k_6 \left(\frac{n}{n_i^2}\right)^2 p_{As_4}^{1/4} \tag{1.6}$$

Similar equations describe the formation and pressure dependencies of arsenic vacancies.

In a confined volume at a given temperature the elements will evaporate until the equilibrium partial pressure is reached. These partial pressures are plotted in figure 1-5 and depend on whether the crystal is As or Ga rich and the temperature. Since As is the more much volatile element and requires more elemental evaporation for a given partial pressure (forming gaseous As_2 or As_4 vs. monatomic Ga), excess As is often added to prevent surface decomposition at higher processing temperatures (Casey and Panish 1968; Palfrey, et al. 1981; Bösker, et al. 1995).

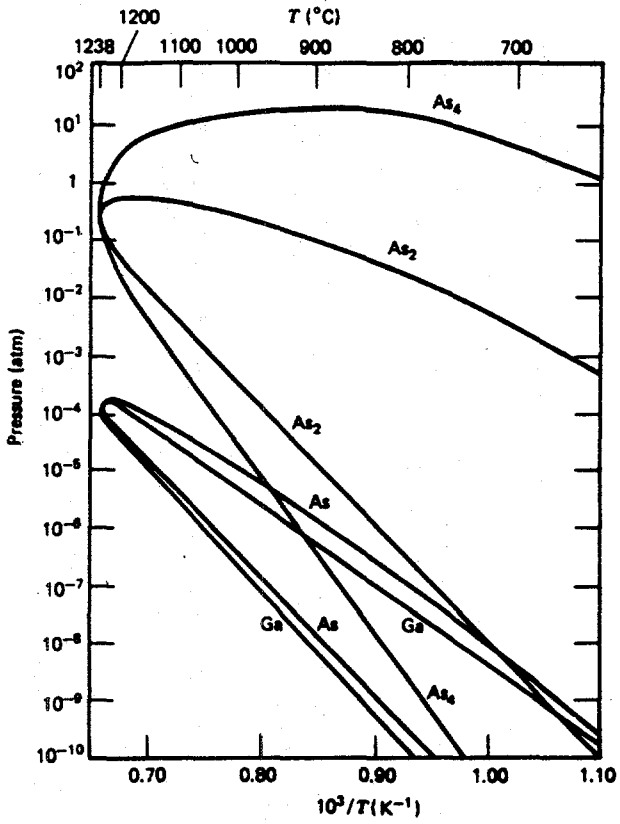

Figure 1-5: The elemental partial pressure over GaAs at equilibrium. The upper half of the Ga curve and lower half of the As curves are for Ga-rich processing and the opposing halves are for As-rich conditions (Arthur 1967).

Chemical impurities are another important source of defects in semiconductor materials. Chemical impurities can be either intentionally added during growth or doping processes or be unintentionally present through contamination of the starting material or process equipment. Chemical impurities can either be substituted onto Ga or As sites or occupy interstitial positions. The positions they occupy as well as their valence determine whether or not they are electrically active as donors or acceptors.

1.3. Related III-V Based Devices

A substantial difference between AlGaAs and Si device processing is that silicon based devices use implantation and diffusion of electrically active impurities to create the active device regions whereas AlGaAs devices rely mainly on deposition and etching to pattern and isolate active devices. Deposition and etching are typically used for the formation of such heterostructures because of the tight spacing of different AlGaAs alloys with varying doping requirements between layers and the atomically flat interfaces required between layers (Ghandi 1994). Some current examples of AlGaAs based devices are Edge Emitting [figure 1-6] and Vertical Cavity Surface Emitting Lasers (VCSELs) [figure 1-7]. Both of these examples use layers deposited by MOCVD or MBE to form the desired sequence of band gaps, band offsets and material doping. Both devices also use etched or cleaved sidewalls to confine photons within the active region. However the use of etched boundaries to create photon confinement limits the possibility of integrating a large number of such devices into an optoelectronic integrated circuits (OEIC) (Yang, et al. 1995). An example of a device that would be more conducive to OEIC use is the transverse junction stripe (TJS) laser [figure 1-8]. This device is an edge-emitting laser with the optical confinement provided by AlGaAs (with a composition having a band gap greater than the device emitted photons), rather than the physical edges of the device.

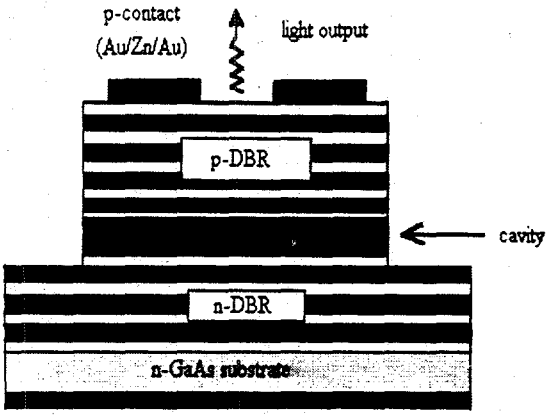

Figure 1-6: Schematic of a Vertical Cavity Edge Emitting Laser (VCSEL) showing the optically active region flanked by distributed Bragg reflector (DBR) mirrors. The DBR mirrors are superlattice structures comprised of AlGaAs layers.

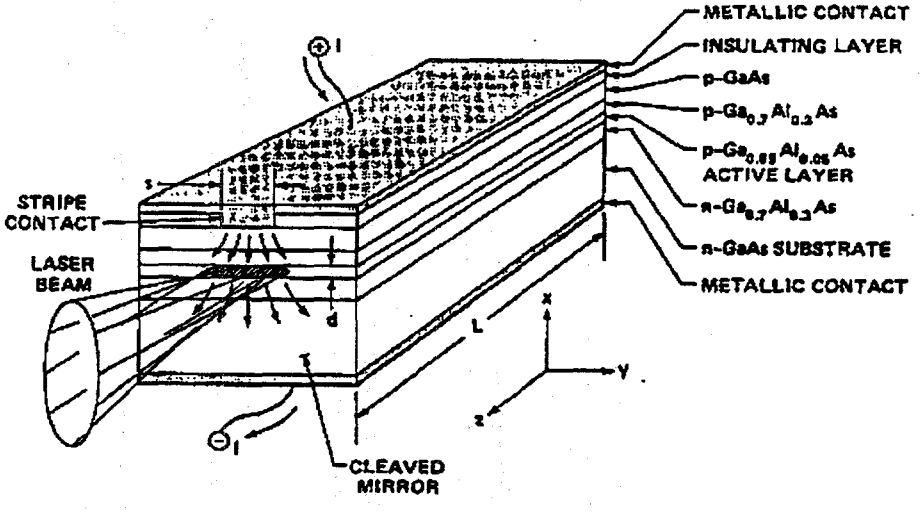

Figure 1-7: Edge emitting AlGaAs laser (Haller 1997)

While the fabrication of TJS lasers still requires MOCVD or MBE growth and etching operations, Zn diffusion steps can reduce the overall processing time and thermal stress on the AlGaAs heterostructures. The use of Zinc as an acceptor impurity species for forming contacts and to produce impurity induced layer disordering (IILD) to form

the photon boundaries of the laser has been demonstrated to dramatically reduce the processing time required at elevated temperatures. For example, the TJS laser structure in figure 1-8 requires just 3 minutes of rapid thermal annealing using Zn diffusion as opposed to 1-3 hours at 600-800°C for conventional process designs. Such extended high temperature diffusions can deleteriously affect the integrity of GaAs/AlGaAs interfaces and thereby alter the wavelength of the photon emission (Laidig 1981).

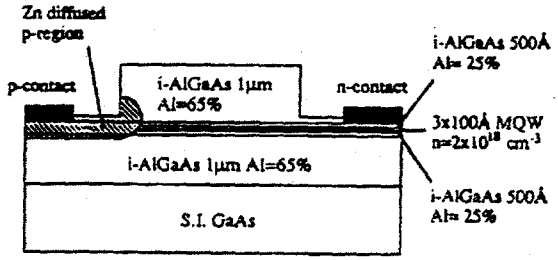

Figure 1-8: Example of a GaAs/AlGaAs heterostructure based device that uses IILD to reduce processing complexity and cost (Yang, et al. 1995)

1.4. Motivation for this Research

Along with the dramatic example of IILD, other electrically active dopants are known to enhance or retard the interdiffusion of AlGaAs/GaAs/AlAs layers (Deppe and Holonyak 1988; Cohen 1995). However, modeling of this behavior has produced seemingly contradictory analysis of the diffusion mechanisms responsible for these results. Interdiffusion in AlAs/AlGaAs/GaAs systems is generally attributed to vacancies on the group III sublattice and is assumed to be a direct result of Ga/Al self-diffusion (Zimmerman, et al. 1993). Enhancement and retardation of the self-diffusion is linked to the position of the Fermi level (governed by the doping level) which determines the equilibrium concentration of vacancies. Predicting the exact effect doping will have on

Ga self-diffusion requires knowledge of the valance and energy levels of the Ga vacancies.

Total energy calculations have predicted that the Ga vacancy with a triple negative charge is the dominant defect in intrinsic and n-type GaAs crystals (Baraff and Schlüter 1985). This conclusion was also reached based on analysis of diffusion experiments using GaAs/AlAs superlattices doped with Si (Tan and Gösele 1987). However other studies report successful modeling of self-diffusion behavior using singly negatively charged Ga vacancies (Li, et al. 1997; Muraki and Horikoshi 1997). To resolve this ambiguity in the charge state of the Ga vacancy along with the lack of definitive model for IILD of GaAs superlattice by Zn diffusion was the goal of this investigation.

1.5. Related Previous Diffusion Studies

There has been a small selection of studies, both experimental and theoretical, investigating the effects of doping on self-diffusion behavior in GaAs/AlAs superlattices. Laidig et al. (1981) first reported IILD of superlattice structures in 1981 using AlAs/GaAs quantum well heterostructures (QWH). After diffusing Zn, the authors observed complete compositional disordering of the superlattice at 575°C after just 10 min. Where the structure was covered by a Si_3N_4 mask no interdiffusion of the layers occurred as opposed to where Zinc was free to enter the samples the AlAs/GaAs layers became completely homogenized into $Al_{x/(x+y)}Ga_{y/(x+y)}As$, where x is AlAs layer thickness and y is the GaAs layer thickness. A dramatic illustration of their work can be seen in figure 1-9.

A more detailed study of similar structures was carried out soon there after (Lee and Laidig, 1984) using secondary ion mass spectroscopy (SIMS) and Auger electron spectroscopy (AES) to measure the interdiffusion of the layers and perform analysis of the interdiffusion. The disordering was found to begin only when the Zn concentration exceeded ~$1x10^{18}$ cm^{-3} and proceeded more than $1x10^{5}$ the rate of disordering compared to when Zn is not present. In this analysis the Zn diffusion and Al-Ga interdiffusion were both found to be dependent on layer thickness even when the average composition of the material was constant. That the diffusion was strongly dependent on the number of interfaces in the samples suggests that the AlAs/GaAs interfaces may not have been ideal.

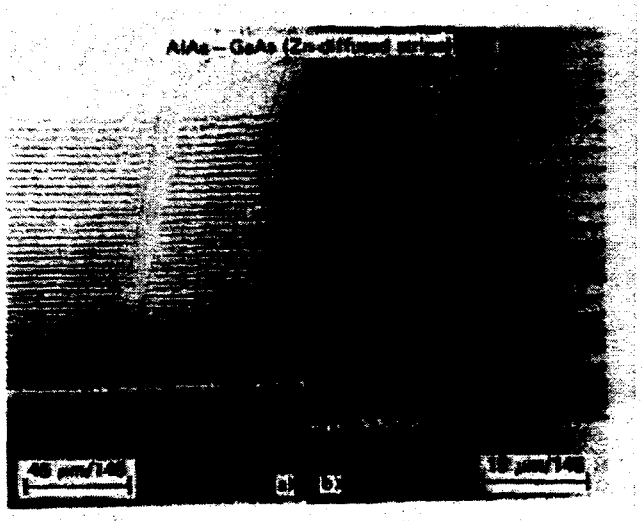

Figure 1-9: The first reported demonstration of impurity induced layer disordering of an AlAs/GaAs superlattice (Laidig, et al. 1981)

Also, while the diffusion coefficients were calculated using error function and Boltzmann-Motano approximation, the analysis is limited by the accuracy of AES and the fact that the Al-Ga interdiffusion profiles are summarized qualitatively by categorizing regions of the samples as having slight, intermediate and total disordering. This work also assumes a constant diffusion coefficient for Zn, which has been widely

reported to have a strong concentration dependence (Casey and Panish 1968; Cohen 1995; Bösker, et al. 1995; Chase, et al. 1996).

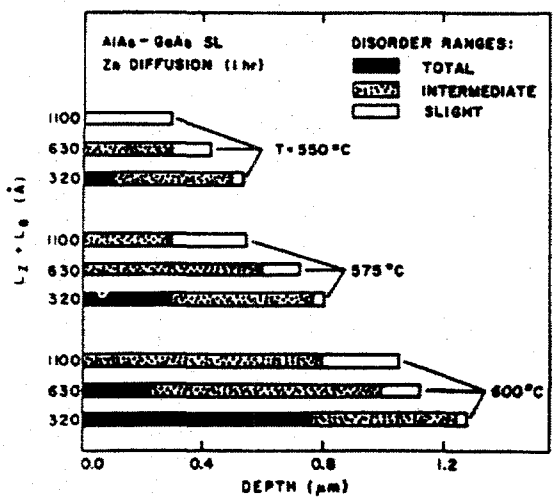

Figure 1-10: Results of Lee and Laidig (1984) qualitatively showing the amount of disordering of three different period lengths of AlAs/GaAs superlattices at three separate temperatures

More recently Ky et al. (1996) has investigated the effect of background Si and Be doping (i.e. growing dopants into the layers) on the IILD of AlAs/GaAs superlattices using a higher Zn surface concentration of ~$1x10^{20}$ cm^{-3}. These SIMS measurements appear more accurate than other experiments and the study also includes detailed analysis of the photoluminescence (PL) transitions in the material. However, various studies of the effects of Zn diffusion show that such high concentrations cause voids and extended defects in the structure (Luysberg, et al. 1992; Jäger, et al. 1993) which act as sinks for the diffusion of interstitials making the overall diffusion analysis of this work somewhat ambiguous.

Because of the dearth of quantitative results and the many unknown parameters there has been only one attempt to completely model the Zn induced disordering of an AlAs/GaAs superlattice (Zimmerman, et al. 1993). This analysis used the qualitative

results of Lee and a set of four coupled partial differential equations to simulate the available data of Lee. Due to the lack of information about Zn diffusion in AlAs, these simulations were based on the assumption that the diffusion rates in AlAs and GaAs were identical. The simulations showed that the enhanced interdiffusion was mainly caused by the p-doping of the Zn causing a reduction in the Fermi level leading to an increase in the equilibrium concentration of the Ga interstitials. Importantly for our studies it was noted that regardless of the ambient conditions, the disordering at the Zn diffusion front initially proceeds under Ga rich conditions but may be influenced by As rich defects at a later stage of the diffusion (Zimmerman, et al. 1993). Separating these two possible influences presents a problem for modeling since all previous experiments were carried out in an As rich ambient and there is no consistent model for the defect formation that occurs during the Ga-rich to As-rich transition. Thus Zimmerman et al. assumed the disordering was completely due to the Ga-rich effects and justified this with simulation profiles qualitatively similar to the Lee data.

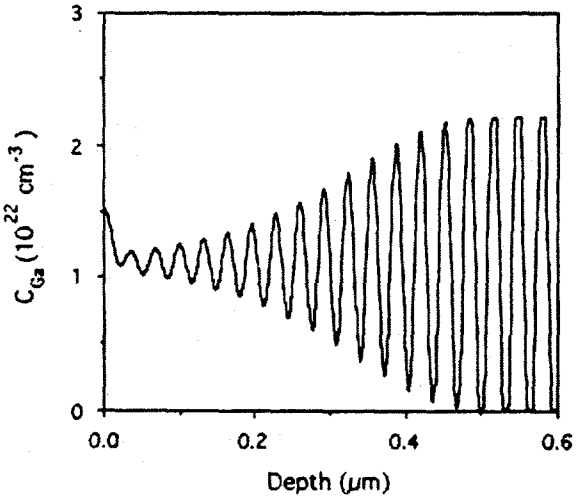

Figure 1-11: Simulation Ga profile caused by Zn induced layer disordering of a AlAs/GaAs superlattice (Zimmerman, et al. 1993)

The authors concluded that of the two possible effects for the superlattice disordering, the Fermi effect and the supersaturation of Ga self-interstitials, the former was the major contributor to IILD.

2. Diffusion

Diffusion describes the fundamental random walk process by which defects and atoms move throughout a crystal lattice. Diffusion describes the motion of constituent atoms of a crystal within that same crystal (self-diffusion), the motion of the constituent atoms of disparate crystals across a junction (interdiffusion), and the motion of chemical defects within a crystal (impurity diffusion). In any of these cases it would be impossible for atoms to move from lattice site to lattice site in a perfect crystal, i.e., atoms need a site to move to for diffusion to take place. Therefore, all diffusion requires there be one or more crystal defects acting as a transport conduit for atom movement, and the diffusivity of a given species is determined by the transport capacity of all possible defects. So

$$D = \frac{1}{C}\sum D_X C_X \tag{2.1}$$

where D is the diffusivity of an atomic species with concentration C, D_X is the diffusivity of a defect X and C_X is the defect concentration. There may be multiple defects that contribute to the overall flux of atoms from once position to another, but for specific conditions one dominant defect can usually be identified. It is the relative abundance of the dominant defect combined with concentration of the diffusing species and the frequency of atomic jumps to the defect site that determine the diffusion rate. Thus identifying and characterizing the dominant defect is a crucial element of understanding and eventually predicting diffusion behavior. In the following subsections a general overview of the three varieties of diffusion mentioned above will be given, followed by a description of how they relate to our experiments. The exact models used to simulate our experiments will be discussed in Chapter 2 with sample results and discussion presented in Chapters 4 and 5, respectively.

While diffusion processes differ greatly in rate and type of the diffusing species, they share a common framework for mathematically describing diffusion through a fixed volume of material. Known as Fick's laws, equations 2.2 and 2.3 do not predict the individual jumps of a specific atom but rather model the overall movement of a given

$$J = -D\frac{\partial C}{\partial x} + Q \tag{2.2}$$

$$\frac{\partial N}{\partial t} = \frac{\partial}{\partial x}\left(D\frac{\partial C}{\partial x}\right) + Q \tag{2.3}$$

species or atomic species. Where J is the atomic flux, D is the diffusivity of the species, Q represents the creation of species via chemical or other reactions, and $\partial N/\partial x$ is the local concentration gradient of the species. Integration of equation 2.1 over a given volume gives a differential of the concentration, C, at a given species at a given location, x, over time, t [2.3].

For most cases the diffusivity, D, is given by

$$D = ga^2 v_o \exp\left(\frac{S}{k}\right)\exp\left(\frac{-H}{kT}\right) = D_0 \exp\left(\frac{-E}{kT}\right) \tag{2.4}$$

where g is a geometric factor specific to the lattice type, a is the lattice constant of the material, ν_0 is the maximum vibrational frequency of an atom, S is the entropy of the self-diffusion configuration, k_B is Boltzmann's constant, and H is the enthalpy of migration. The diffusivity is commonly written as the amalgamation of constants combined with the enthalpy of defect formation described with an activation energy E.

$$D = D_0 \exp\left(\frac{-E}{kT}\right) \tag{2.4a}$$

Even though the vibrational frequency is somewhat temperature dependent, D_o is taken as a constant since D is dominated by the exponential dependence on temperature.

If the diffusing species has a charge and there is an electric field created by ba offsets, doping above the intrinsic carrier concentration, or other means, there is additional component to the atomic motion caused by the electrostatic force on the atc and interaction with the charged defect species.

Under steady state conditions the directional drift velocity added to the random walk jump motion is given by equation 2.5 where Z is the ionic valence, q is the charge on one e^-, $\vec{E}$ is the electric field and μ is the mobility of the ionized species.

$$v_d = ZqE = \mu\vec{E} \qquad (2$$

The flux of the ionized species is then described by

$$J = -D\frac{\partial C}{\partial x} + \mu C\vec{E}(x) + Q \qquad (2$$

where C is the concentration of a given species.

These are the most basic forms of the diffusion equations and apply to syste where D is independent of concentration and where there are no grain boundaries surface effects (such as stress or oxide formation) to inject or sink defects.

The Fermi level of the sample can affect the diffusivity by a change in the equilibrium concentration of defects in the crystal. For example the formation of a vacancy with a j- charge

$$V^o + je^- \Leftrightarrow V^{j-} \qquad (2$$

determines that the equilibrium concentrations are given generally by

$$r = \frac{\left[V^{j-}\right]}{\left[V^o\right]\left[e^-\right]^j} \qquad (2$$

where r is the reaction constant under particular doping conditions. For extrinsic and intrinsic conditions this relationship simplifies to

$$r^{\text{extrinsic}} = \frac{[V^{j-}]}{[V^o][n]^j} \quad and \quad r^{\text{intrinsic}} = \frac{[V^{j-}]}{[V^o][n_i]^j} \tag{2.8a}$$

Dividing $r^{extrinsic}$ by $r^{intrinsic}$ gives

$$\frac{[V^{j-}]}{[V^0]} = \left(\frac{n}{n_i}\right)^j \tag{2.9}$$

which means that the movement of the Fermi level towards the conduction band increases the equilibrium concentration of V^{j-} (Longini and Greene 1956). Assuming the diffusion coefficient of a given defect does not change with the Fermi level, the diffusivity is influenced solely by the change in equilibrium concentration of defects. Thus the extrinsic conditions can be related to the intrinsic case via equations 2.10.

$$(a) \quad D_{SD}^{\text{extrinsic}} = D_{SD}^{\text{intrinsic}}\left(\frac{n}{n_i}\right)^j \quad (b) \quad D_{SD}^{\text{extrinsic}} = D_{SD}^{\text{intrinsic}}\left(\frac{p}{n_i}\right)^k \tag{2.10}$$

for (a) negatively, j-, and (b) positively, k+, charged defects respectively.

2.1. Self-diffusion

Self-diffusion is the most basic all of diffusion cases involving only the movement of the constituent atoms of a material within a given volume. Assuming the material is homogenous, there are no chemical concentration gradients driving the diffusion process and the movement of atoms is only dictated by random walk movements. Without some method of marking atoms the material will be indistinguishable from its original state even after large amount of diffusion has occurred.

The self-diffusion coefficient of a given species results from the combined contributions of all charge states (neutral, j and k) of all defect species X, as the concentrations depend on the doping level in the crystal [2.11].

$$D^{SD} = \frac{1}{C}\sum_X \left(C_X^o D_X^o + \sum_j C_X^{j-} D_X^{j-} \left(\frac{n}{n_i}\right)^j + \sum_k C_X^{k+} D_X^{k+} \left(\frac{p}{n_i}\right)^k \right) \qquad (2.11)$$

For self-diffusion in AlGaAs compounds the possible defects are vacancies or interstitials. The dominant defects under n- and p-type doping conditions have been determined previously by the dependence of self diffusion on the As partial pressure (Olmsted and Houde-Walter 1992) or doping (Yu, et al. 1991; Bösker, et al. 1995) .For group III self-diffusion, vacancies dominate under n-type doping while self interstitials dominate under p-type doping. Using the self-diffusion coefficient measured under intrinsic conditions in undoped samples and the doping level in the sample, the charge states of the contributing defects can be determined from such non-equilibrium diffusion experiments.

2.2. Interdiffusion

Closely related to self-diffusion is the diffusion of two materials across a boundary. In the case of the interdiffusion of Al and Ga between AlGaAs and GaAs, the interdiffusion coefficient is described by equation 2.12

$$\tilde{D} = (N_{Ga} D_{Al} + N_{Al} D_{Ga}) \Phi S \qquad (2.12)$$

(Manning, 1961; Darken, 1984) where N is the mole fraction of each species, D is the diffusion of each species, Φ is a thermodynamic factor, and S is the correlation factor. The correlation factor accounts for the fact that if the interdiffusion proceeds by a lattice atom moving to an adjoining vacancy there is a greater probability of the atom returning to its now vacant prior site than to any other nearest neighbor site. In the absence of prior information, D_{Al} and D_{Ga} can not be separated from ΦS by measuring the interdiffusion

coefficient. In all prior work it is assumed that $\Phi S=1$ (Olmsted and Houde-Walter 1992; Zimmerman, et al. 1993) and that the diffusion coefficients are identical giving $\tilde{D}=D_{Ga}$. Using $Ga^{69}As/Ga^{71}As$ superlattice structures the interdiffusion coefficient reduces to $\tilde{D}=D_{Ga}\Phi S$ and information about ΦS product can be deduced.

2.3. Impurity Diffusion

In the prior section discussing self-diffusion in the bulk lattice we assumed that there is no charge on the diffusing atoms. However, for device fabrication, impurities are often added specifically because they are easily ionized, i.e., for doping of the material n- or p-type. Assuming the impurities are completely ionized (generally assumed for shallow donors/acceptors at any temperature where diffusion would be significant), impurity diffusion proceeds according to equation 2.6 with the charge state of the dominant species and local electric field becoming critical components for predicting the diffusion behavior.

2.3.1. Zinc Diffusion in GaAs

Zinc is one of the most commonly used impurities for p-type doping because of its low ionization energy, short diffusion time and high solubility in AlGaAs. Since the early 1960s there have been many studies of the diffusion behavior of Zn in GaAs with various mechanisms proposed to explain the experimental results. It is believed that Zn diffuses in GaAs via the kick-out mechanism (Yu, et al. 1991) with Zn atoms moving interstitially through the lattice before assuming sites on the Ga lattice by displacing

(kicking-out) a substitutional Ga atom (Ga_s) thus creating a Ga self interstitial (Ga_I) [2.13].

$$Zn_i^+ + Ga_s^o \xleftrightarrow{r_f, r_r} Zn_s^- + Ga_I^{k+} + (k-2)h^+ \qquad (2.13)$$

The k+ denotes multiple possible charge states, 2 or 3, of the Ga self-interstitial and $r_{f,r}$ are the forward and reverse rate of reactions, respectively. While there is some additional component to the diffusion from substitutional Zn moving via vacancies in the Ga sublattice, it is negligible compared to the contribution of the interstitial diffusion. At any given time most of the Zn occupies substitutional Ga sites forming a shallow acceptor, while the interstitials at much lower concentration form deep donors. The substitutional Zn concentration, C_s, creates a net hole concentration, p, of

$$p = \frac{1}{2}\left[C_s + (C_s^2 + 4n_i^2)^{1/2}\right] \qquad (2.14).$$

This doping moves the Fermi level towards the valence band which in turn increases the equilibrium concentration of Ga self-interstitials, $C_I(p)$, relative to the concentration under intrinsic conditions, $C_I(n_i)$ [2.15]. A similar relationship describes the Zn interstitial concentration in p-type crystals.

$$C_{I^{k+}}(p) = C_{I^{k+}}(n_i)\left(\frac{p}{n_i}\right)^k \qquad (2.15)$$

The consequences of the kick out mechanism are made more apparent by the definition of R_k as the ratio of the transport capacity of Ga self-interstitials with a charge k+ to that of Zn interstitials (Yu et al. 1991).

$$R_k \equiv \frac{D_k C_k(p)}{D_i C_i(p)} \qquad (2.16)$$

where D_k and D_i are the diffusivities of the interstitial species. The magnitude of R_k indicates the rate-limiting step of the kick-out reaction. The reaction can be visualized as the trade off between movement of Zn interstitials deeper into the sample versus the Ga interstitials moving toward the sample surface where the equilibrium Ga interstitial concentration is higher. R_k is assumed to be dominated by the concentration terms since the speed of individual interstitial movement is dominated by the temperature dependent hopping frequency.

For $R_k >> 1$ the rate determining process in the kick-out reaction is the incorporation of Zn interstitials from the sample surface because the high p-doping creates a high equilibrium concentration of Ga interstitials near the surface. In general this condition occurs when the Zn concentration is near the solubility limit. This condition leads to an effective diffusivity of the Zn that is dependent on the local substitutional Zn concentration squared. [2.17]

$$D_{eff} \approx \frac{2C_i^{eq}(p)D_i}{C_s^{eq}}\left(\frac{C_s(x,t)}{C_s^{eq}}\right)^2 \tag{2.17}$$

For $R_2 << R_3 << 1$ the movement of the Ga interstitials away from the diffusion front is the rate limiting process and a supersaturation of Ga interstitials occurs. In this case the effective Zn diffusivity is inversely proportional to the local substitutional Zn concentration [2.18].

$$D_{eff} \approx \frac{2C_I^{eq}(p)D_I}{C_s^{eq}}\left(\frac{C_s^{eq}}{C_s(x,t)}\right) \tag{2.18}$$

If the rate limiting step is the transport of I^{3+}, $R_2 << R_3 << 1$, then the Zn diffusivity is independent of the local Zn concentration and thus described by an error function profile. Profiles

such as the one seen in figure 2.1 have been attributed to Zn diffusion, rate limited by the combination of both I_{Ga}^{2+} and I_{Ga}^{3+} removal from the diffusion front.

Because of the possible dependence on concentration, Zinc diffusion into GaAs can not be modeled in most cases using a simple error function (Gösele and Morehead 1981). If the Zn diffusivity is described by equation 2.12 under Ga-rich conditions the result is a so-called box shaped diffusion profile. If the same Zn diffusion is performed in an As-rich atmosphere, a so-called "kink and tail" profile occurs because the Zn solubility is higher under As-rich conditions. However, the As-rich condition does not extend very far into the crystal. Thus there are distinct box-shaped profiles in both the Ga and As rich regions superimposed forming the kink and tail profile (Yu, et al. 1991). These two types of profiles have been generally seen in profiles where the Zn surface concentration exceeds 10^{20} cm^{-3}.

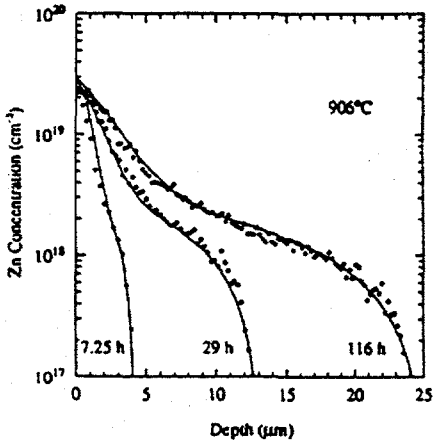

Figure 2-1. Zn diffusion in GaAs using dilute Zn source to a Zn surface concentration below the saturation level (Bösker, et al. 1995)

2.4. Experimental Methods of Measuring Ga and Zn Diffusion in AlGaAs

While self-diffusion may be the simplest process to envision and model, it is certainly the most difficult to measure. Whereas the dissolution of a distinct interface

between two materials and the penetration of a foreign atom into a material provides obvious and measurable evidence of diffusion, self-diffusion provides no such measurable alteration in the bulk material composition. To measure self-diffusion atoms must be "marked" to allow for measurement of their movement directly or the inert markers need to be placed in the material to deduce the self-diffusion behavior indirectly.

2.4.1. Radiotracer Measurements

Since self-diffusion measurements were first performed, the in-diffusion of radioactive isotopes from the surface has been a widely used approach. In a typical experiment, radioactive isotopes of one of the host lattice species are deposited or implanted to create marker atoms for the self-diffusion. The samples are annealed to diffuse the radioisotope into the material. Finally the concentration profile of the radioisotope is measured. Since the half-life, amount of radioactive material introduced and time since deposition are all known, there is predictable amount of radioactivity now in the sample. By measuring the distribution of this radioactivity either by sputtering or etching the sample at a known rate, a radiotracer self-diffusion profile can be obtained.

There are a number of problems with this technique that limit its efficacy and accuracy. First, from a practicality standpoint the use of radioactive isotopes is undesirable because the isotopes may be hazardous, require specialized lab equipment, dedicated lab space, and appropriate protective clothing, gloves, etc. Second, the set of available atoms that can be examined with these studies is limited to those atoms with radioactive isotopes which are readily available, not too toxic, capable of being deposited or implanted and have a half life of an order of magnitude similar to the desired annealing

time. Diffusion depths also need to be appropriate for the sputter or etching capability used to analyze the profiles. Diffusion of Zn into AlGaAs alloys using this method has been done (Boltaks, et al. 1975). The results showed kink and tail diffusion profiles over large (>25μm) distances.

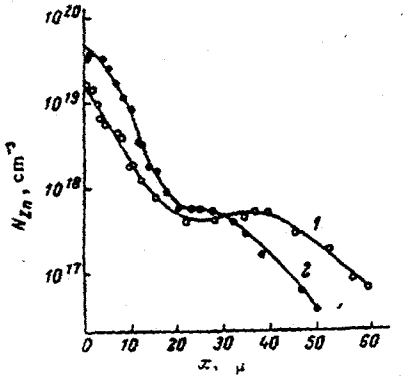

Figure 2-2: Radiotracer measurements of Zn diffusion into GaAs using a low Zn surface concentration (Boltaks, et al. 1975)

In addition to the issues related to radioactivity, the radiotracer method requires introduction of material from one of the sample boundaries usually by ion implantation or deposition. Implantation induces damage (and thus defects), and deposition is very susceptible to surface contamination such as oxygen or other impurities at the surface, both of which can dramatically influence the self-diffusion rate. Accurate studies of compound semiconductors also require that the deposited/implanted material maintain the stoichiometry of the bulk material lest concentration gradients be created at the surface. An extreme example of results influenced by these various experimental errors can be found in an investigation of self-diffusion with radioactive Ga and Sb used for radiotracer measurements of self diffusion in GaSb (Weiler and Mehrer 1984). Even with

a careful experimental set up, the results obtained by three different groups vary by nearly six orders of magnitude (figure 2-3).

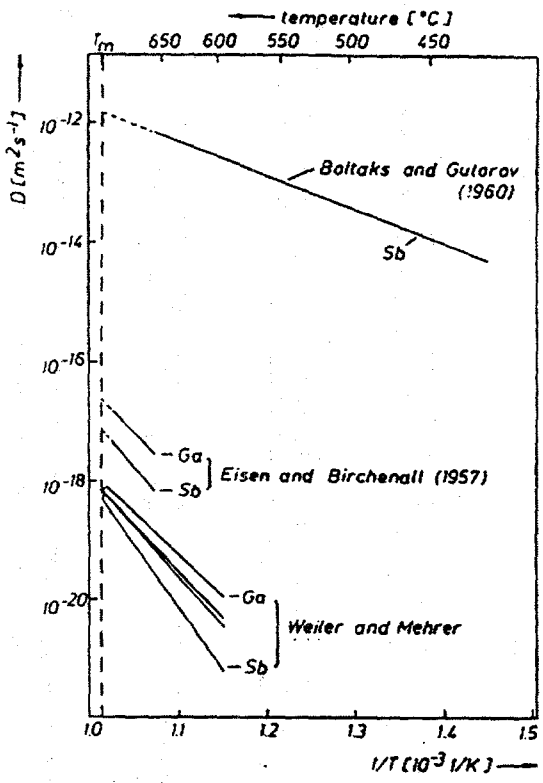

Figure 2-3. The self-diffusion coefficients of Ga and Sb in GaSb as determined by different groups using the radiotracer technique (Weiler and Mehrer 1984)

2.4.2. Isotopically Enriched Samples

A relatively new approach for measuring self-diffusion uses isotopically enriched multilayer structures (Haller, 1995). Many elements exist in nature as a mixture of several stable isotopes and the fraction of each isotope is generally consistent throughout the globe. Using gas centrifuges or other means individual isotopes can be selectively enriched and material can thus be created with any desired fraction of specific isotopes. Large quantities of highly enriched isotopes were first used in WWII for nuclear weapons.

Isotopically enriched multilayer structures of GaAs were used to measure Ga self-diffusion for the first time in 1992 (Tan et al. 1992). The authors questioned their own results suggesting that their attempt to measure the intrinsic self-diffusion coefficient was influenced by the high Si doping of the substrate which may have affected the native defect concentration and the diffusion in the superlattice structure. Undoped isotope epi-layers grown on SI GaAs substrates were employed to measure Ga self-diffusion and produced more consistent results which are in excellent agreement with molecular dynamics calculations (Wang, et al. 1997; Bracht, et al. 1998). Isotopically enriched structures have also been used to study self-diffusion in other undoped and doped III-V systems including GaP (Wang, Wolk, et al. 1997), GaN (Ambacher, Freudenberg, et al. 1999) and most recently GaSb (Bracht, et al., to be published) as well as in the conventional group IV semiconductor Si (Bracht, et al.1998) and Ge (Fuchs, et al 1995).

2.4.3. Junction Depth Measurements

One of the simplest methods to measure the diffusion depth of electrically active impurities is to diffuse a p-type (n-type) dopant into an n-type (p-type) substrate. The sample is then cleaved and an etchant is used to delineate the p-n junction, where the concentration of the dopant equals the background doping level of the substrate. The diffusion behavior is assumed to be described by an error function profile with an effective diffusion coefficient, D_{ef}, given by equation 2.19.

$$D_{effective} = \frac{d^2}{4t} \tag{2.19}$$

where d is the junction depth and t is the time. Though this technique has been used to study Zn diffusion in GaAs (Shih, 1976) and InGaAs (Urisu, et al. 1976), and provides a

practical metric for device fabrication, it does not provide any information about the profile shape and mechanism of the Zn diffusion.

2.4.4. Closed Ampoule Annealing

The experimental method widely used for diffusion research, regardless of sample type, is the "closed ampoule" technique. The samples and other sources are placed within an evacuated quartz ampoule and are subjected to the desired annealing temperatures and duration. Though this method is generally impractical for commercial production, it is a valuable experimental method because the temperature, pressure, and composition of a system can be easily and accurately controlled.

Historically, various sources have been used to create a Zn overpressure above the GaAs samples during closed ampoule annealing. Zn doped silica films, elemental Zn with or without elemental As (Urisa and Kajiyama 1976), $ZnAs_2$ and Zn_3As_2 (Casey and Panish, 1968; Shih, 1976;) have all been documented to produce a satisfactory Zn overpressure without damaging the sample surfaces. Silica films provide control over the surface Zn concentration but introduce stress and hence defects at the surface so they are not ideal for diffusion studies (Cohen 1995). $ZnAs_2$ and Zn_3As_2 have often been used because it produces very repeatable results. At a given temperature these compounds can be used to define a region of three condensed phases in the Ga-As-Zn ternary phase diagram. For an isothermal system the degrees of freedom are given by the phase rule

$$F=3-P \qquad (2.20)$$

Where P is the number of phases in the system and F is the number of degrees of freedom which are undetermined by the experimental conditions. If for example both Zn_xAs_y alloys are placed with a GaAs sample at 700°C, the degree of freedom is zero and the system is in region G of figure 2-4 (Casey and Panish 1968).

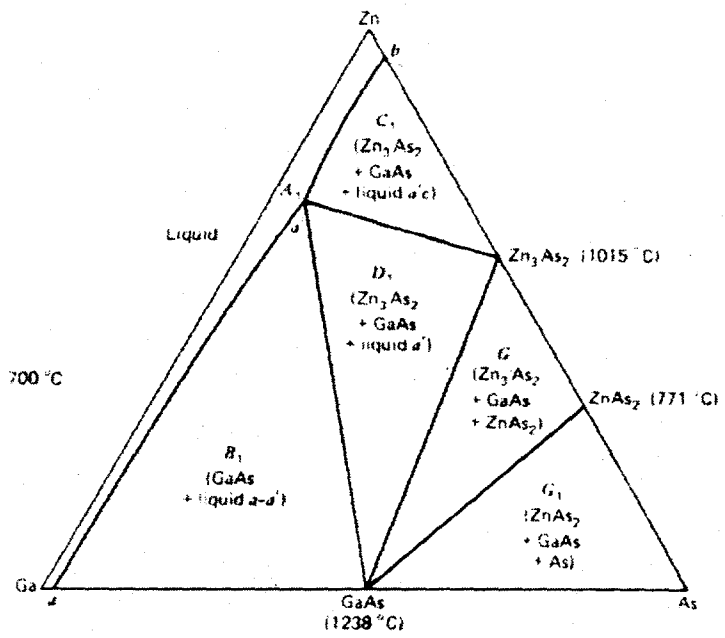

Figure 2-4: The ternary Ga-As-Zn phase diagram at 700°C (Ghandi 1994)

Since the three equilibrium phases are all in condensed form, the equilibrium partial pressure of all components is determined irrespective of the amount of each compound present. The Zn surface concentration is also independent of the amount of source material added and the diffusion profiles are determined solely by the annealing time of the samples at a given temperature. An important consideration for this work is that the use of these solid sources at temperatures of 550-800°C produces Zn surface

concentrations of $>10^{20}$ cm^{-3} which has been observed to cause voids and other extended defects in GaAs making diffusion measurements very difficult.

Ga-Zn alloys have also been used for Zn diffusion sources placing the overall system in region B_1 of figure 2-5 (Kendall and Bartning 1977). In this case the Zn vapor pressure is not solely based on temperature but depends on the amount of alloys added to the ampoule. Since the Zn vapor pressure determines the Zn surface concentration, this method allows control of the surface concentration by variation in the amount of alloy added to the ampoule.

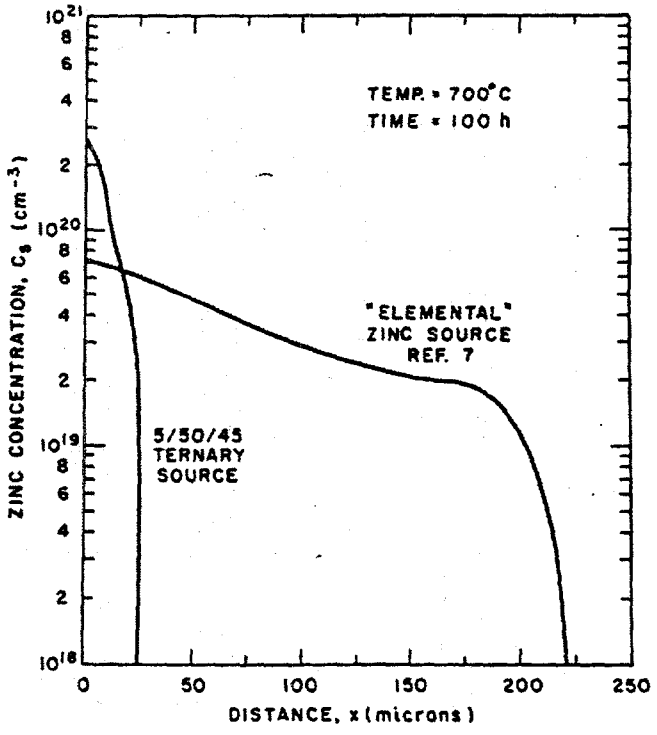

Figure 2-5: At a constant temperature the choice of diffusion source has a dramatic effect on Zn diffusion surface concentration and thus the profile shape is dramatically different. The high Zn partial pressure of Zn/Ga/As ternary sources leads to diffusion profiles with a higher surface concentration but shorter penetration depth compared to elemental Zn or Ga-Zn alloy sources (Casey and Panish 1968).

2.5. Comprehensive Diffusion Models

2.5.1. GaAs SL Disordering Modeling

The kick-out model [2.13] was used for modeling of the Zn diffusion into the GaAs superlattice. Since by the nature of in-diffusion the Zn doping is not uniform, the atomic flux proceeds under the influence of a dopant gradient generated electric field [2.6]. Using the definition of an electric field

$$\vec{E}(x) = -\frac{\partial \psi}{\partial x} \tag{2.21}$$

where ψ is the potential, with the derivative of the local free electron concentration is given by

$$\frac{\partial n(x)}{\partial x} = N_C \exp\left(\frac{E_F - E_C + e\psi(x)}{kT}\right)\frac{e\dfrac{\partial \psi}{\partial x}}{kT} \tag{2.22}.$$

From equation 2.22 we obtain

$$\vec{E}(x) = -\frac{kT}{e}\cdot\frac{1}{n(x)}\cdot\frac{\partial n(x)}{\partial x} \tag{2.23}.$$

Using the Einstein relation

$$\mu = Ze\frac{D}{kT} \tag{2.24}$$

and equation [2.22], the electric field is given by

$$\vec{E}(x) = -\frac{ZD}{\mu}\frac{1}{n(x)}\cdot\frac{\partial n(x)}{\partial x} \tag{2.25}.$$

Substituting this into equation [2.6] the flux of a charged species is given by

$$J = -D\frac{\partial C}{\partial x} - ZCD\frac{1}{n(x)}\cdot\frac{\partial n(x)}{\partial x} + Q \tag{2.26}$$

or to make it more useable for p-type doping the carrier concentration relationship $np=n_i^2$ can be used leading to

$$J = -D\frac{\partial C}{\partial x} - ZCD\frac{1}{p(x)}\cdot\frac{\partial p(x)}{\partial x} + Q \qquad (2.27).$$

Expanding Fick's second law [2.3] for each component of the kick-out diffusion [2.13] using *i* to denote Zn interstitials, *I* for Ga interstitials, *s* for substitutional Zn atoms and *o* to denote Ga atoms on the Ga lattice site we obtain

$$\frac{\partial C_{s^-}}{\partial t} = \frac{\partial}{\partial x}\left(D_S\frac{\partial C_{s^-}}{\partial x} - \frac{C_{s^-}D_S}{p}\frac{\partial p}{\partial x}\right) + r_+C_{i^+}C_0 - r_-C_{s^-}C_{I^{2+}} \qquad (2.28a)$$

$$\frac{\partial C_{i^+}}{\partial t} = \frac{\partial}{\partial x}\left(D_i\frac{\partial C_{i^+}}{\partial x} - \frac{C_{i^+}D_i}{p}\frac{\partial p}{\partial x}\right) - r_+C_{i^+}C_0 + r_-C_{s^-}C_{I^{2+}} \qquad (2.28b)$$

$$\frac{\partial C_{I^{2+}}}{\partial t} = \frac{\partial}{\partial x}\left(D_I\frac{\partial C_{I^{2+}}}{\partial x} - \frac{2C_{I^{2+}}D_I}{p}\frac{\partial p}{\partial x}\right) + r_+C_{i^+}C_0 - r_-C_{s^-}C_{I^{2+}} \qquad (2.28c).$$

By defining normalized variables in [2.29] relating the extrinsic parameters to the intrinsic conditions, the calculations are made simpler.

$$\tilde{C}_s \equiv \frac{C_s}{C_s^{eq}} \qquad (2.29a)$$

$$\tilde{C}_i \equiv \frac{C_i}{C_i^{eq}} \qquad (2.29b)$$

$$\tilde{C}_I \equiv \frac{C_I}{C_I^{eq}} \qquad (2.29c)$$

$$\tilde{n}_i \equiv \frac{n_i}{C_s^{eq}} \qquad (2.29d)$$

This simplification makes the doping dependence implicit in the species concentrations rather than an explicit. This, in turn, reduces the number of input parameters in the

modeling. Further simplification is obtained by reducing the number of rate terms using the necessary conditions for reaction equilibrium [2.30].

$$\frac{r_+}{r_-} = \frac{C_s^{eq} C_I^{eq}}{C_i^{eq} C_o} \tag{2.30}$$

Substituting [2.29] and [2.30] into [2.28] and a more exact description of the p doping which considers the compensation of the Zn acceptors by interstitials

$$p = \frac{1}{2}\left[(C_s - C_i - 2C_I) + \sqrt{(C_s - C_i - 2C_I)^2 + 4n_i^2} \right] \tag{2.31}$$

and excluding the charge superscripts for readability gives the following set of 3 coupled partial differential equations.

$$\frac{\partial \tilde{C}_s}{\partial t} + \frac{\partial}{\partial x}\left(- D_S \frac{\tilde{C}_s}{\sqrt{\left(\tilde{C}_s - \frac{C_i^{eq}}{C_s^{eq}}\tilde{C}_i - 2\frac{C_I^{eq}}{C_s^{eq}}\tilde{C}_I\right)^2 + 4\tilde{n}_i^2}} \frac{\partial\left(\tilde{C}_s - \frac{C_i^{eq}}{C_s^{eq}}\tilde{C}_i - 2\frac{C_I^{eq}}{C_s^{eq}}\tilde{C}_I\right)}{\partial x} - D_S \frac{\partial \tilde{C}_s}{\partial x} \right) \tag{2.31a}$$

$$= r_- C_I \left(\tilde{C}_i - \tilde{C}_s \tilde{C}_I\right)$$

$$\frac{C_I^{eq}}{C_s^{eq}}\frac{\partial \tilde{C}_i}{\partial t} + \frac{\partial}{\partial x}\left(\frac{C_I^{eq} D_i}{C_s^{eq}} \frac{\tilde{C}_i}{\sqrt{\left(\tilde{C}_s - \frac{C_i^{eq}}{C_s^{eq}}\tilde{C}_i - 2\frac{C_I^{eq}}{C_s^{eq}}\tilde{C}_I\right)^2 + 4\tilde{n}_i^2}} \frac{\partial\left(\tilde{C}_s - \frac{C_i^{eq}}{C_s^{eq}}\tilde{C}_i - 2\frac{C_I^{eq}}{C_s^{eq}}\tilde{C}_I\right)}{\partial x} - \frac{C_i^{eq} D_i}{C_s^{eq}}\frac{\partial \tilde{C}_i}{\partial x} \right) \tag{2.31b}$$

$$= r_- C_I \left(\tilde{C}_i - \tilde{C}_s \tilde{C}_I\right)$$

$$\frac{C_I^{eq}}{C_s^{eq}}\frac{\partial \tilde{C}_I}{\partial t} + \frac{\partial}{\partial x}\left(2\frac{C_I^{eq} D_i}{C_s^{eq}} \frac{\tilde{C}_I}{\sqrt{\left(\tilde{C}_s - \frac{C_i^{eq}}{C_s^{eq}}\tilde{C}_i - 2\frac{C_I^{eq}}{C_s^{eq}}\tilde{C}_I\right)^2 + 4\tilde{n}_i^2}} \frac{\partial\left(\tilde{C}_s - \frac{C_i^{eq}}{C_s^{eq}}\tilde{C}_i - 2\frac{C_I^{eq}}{C_s^{eq}}\tilde{C}_I\right)}{\partial x} - \frac{C_I^{eq} D_I}{C_s^{eq}}\frac{\partial \tilde{C}_i}{\partial x} \right) \tag{2.31c}$$

$$= r_- C_I \left(\tilde{C}_i - \tilde{C}_s \tilde{C}_I\right)$$

To determine the movement of the Ga atoms during the Zn diffusion Fick's second law again gives us the partial differential equation that needs to be solved [2.32].

$$\frac{\partial C_{Ga}}{\partial t} = \frac{\partial}{\partial x} D_{Ga} \frac{\partial C_{Ga}}{\partial x} \tag{2.32}$$

Assuming that vacancy diffusion is negligible, the flux of Ga atoms equals the flux of interstitials multiplied by the correlation factor $\Phi_{I_{Ga}}$ [2.33].

$$D_{Ga} C_{Ga} = \Phi_{I_{Ga}} C_{I_{Ga}} D_{I_{Ga}} \tag{2.33a}$$

Rearranging terms gives the Ga diffusivity in terms of the same parameters used in equations 2.31 where the Ga diffusivity is given by the product of the correlation factor, the effective diffusivity of the Ga self interstitials, the fraction of Ga site lattice occupied by Zn atoms, and the saturation concentration of Ga interstitials [2.33b].

$$D_{Ga} = \phi_{I_{Ga}} \frac{C_{I_{Ga}} D_{I_{Ga}}}{C_0} = \phi_{I_{Ga}} \frac{C^{eq}_{I_{Ga}} D_{I_{Ga}}}{C_0} \frac{C_I}{C^{eq}_{I_{Ga}}} = \phi_{I_{Ga}} \frac{C^{eq}_{I_{Ga}} D_{I_{Ga}}}{C^{eq}_{Zn_s}} \frac{C_{Zn_s}}{C_0} \frac{C_I}{C^{eq}_{I_{Ga}}} = \phi_{I_{Ga}} D_I^* \frac{C_{Zn_s}}{C_0} \tilde{C}_{I_{Ga}} \tag{2.33b}$$

This transforms [2.32] into

$$\frac{\partial \tilde{C}_{Ga}}{\partial t} = \Phi_{I_{Ga}} D_I^* \frac{C^{eq}_{Zn_s}}{C_o} \frac{\partial}{\partial x} \tilde{C}_I \frac{\partial \tilde{C}_{Ga}}{\partial x} \tag{2.34}$$

for each Ga species and together with [2.31] and [2.34] defines the five coupled partial differential equation (CPDE) that were solved mathematically to define diffusion in the system.

3. Experimental.

As discussed in Chapter 2 isotopically enriched structures are ideal to explore diffusion behavior. The structures and processing used for these studies were chosen based on the availability of isotope material, the relevance to device technology, and by examining results of previous diffusion studies reported in the literature.

3.1. As-grown Sample Structures.

All the heterostructures used for our studies were grown by molecular beam epitaxy (MBE). The enriched isotopes were obtained with the help of Dr. V. Ozhogin at the Kurchatov Institute in Moscow and the heterostructures were grown by the group of Dr. Karl Eberl and Prof. Manuel Cardona at the Max-Planck-Institute (MPI) in Stuttgart, Germany. Natural gallium consists of two stable isotopes which can be used as markers. ^{69}Ga has 38 and ^{71}Ga has 40 neutrons in the nucleus. ^{69}Ga comprises approximately 60% of the Ga atoms found in nature. Aluminum and arsenic are both mono-isotopic and thus direct self-diffusion measurements can't be made using the isotope technique for these species. However, by assuming that the Ga/Al movements are confined exclusively to the Ga sub-lattice and As movements to its own sublattice, calculation of the Al self-diffusivity in AlGaAs also is a possibility. It is very difficult to measure self-diffusion on the As sub-lattice and, though not considered in this work, it is interesting to note that various experiments with other gallium based III-V systems have shown that diffusion on the group V sub-lattice to be 100-1000x slower than on the Ga sub-lattice.

3.1.1. GaAs Superlattice Structures.

Two different GaAs superlattice structures were used in these studies. Each sample was comprised of 10 periods of double epi-layers. In each period a 50 nm thick GaAs layer containing 99.9% ^{69}Ga was grown followed by a 50 nm layer of GaAs containing 99.9% ^{71}Ga. Both structures were grown on semi-insulating GaAs substrates.

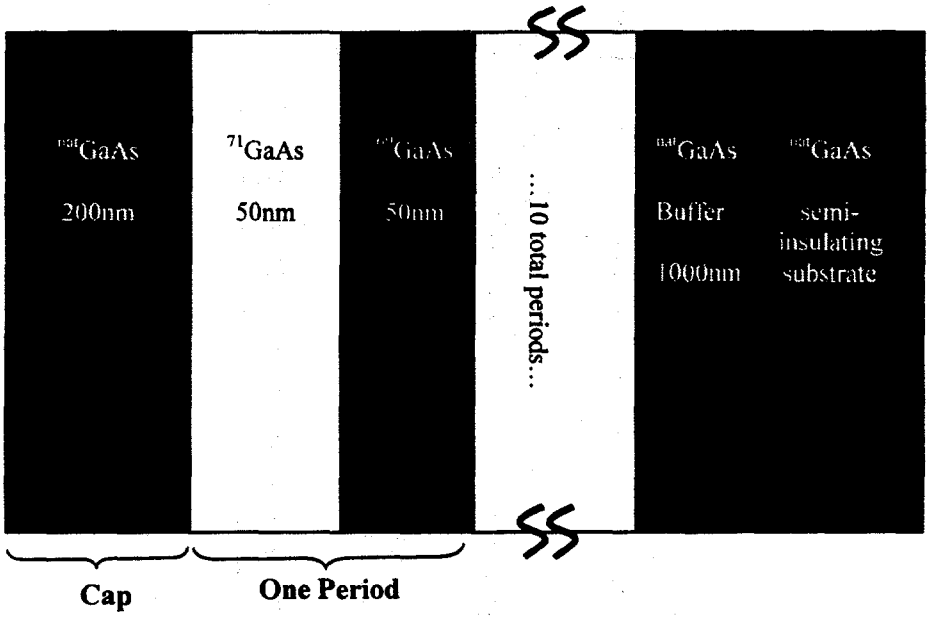

Figure 3-1: General schematic of GaAs isotope superlattice structures used in this work. One period is approximately 100nm thick containing a sequence of ^{71}GaAs followed by ^{69}GaAs. Sample GaAs2 did not have a capping layer or buffer layer of natural composition.

Sample GaAsSL1 was grown at two separate MBE growth temperatures (580°C for the first 5 period and 200-300°C for the second 5 periods), was initiated with a 1000 nm GaAs buffer layer, and was terminated with a 200nm thick GaAs cap layer with Gallium having the natural isotope ratio (^{nat}GaAs) in this layer. In sample GaAsSL2 all periods were grown at the same temperature (580°C), no buffer layer was used between the substrate and the isotope layers and no cap layer was used to terminate the structure.

Assuming the background pressure and purity of the system were similar for the two growths, we expect that in sample GaAsSL1 the addition of a buffer layer produced more crystallographically perfect superlattice layers initially and that the low growth temperature froze in a higher vacancy concentration in the later periods. In sample GaAsSL2 the epitaxy of the isotope layers should be less perfect initially but the consistent high growth temperature should yield more perfect enriched isotope layers (i.e., low vacancy concentrations) near the surface. Because of the limited amount of material (approximately 2-4 cm^2 total of each sample) and complications that dramatically different vacancy concentrations would have presented for modeling, sample GaAsSL1 was used for development and testing of the experimental methods. Sample GaAsSL2 was used for the actual quantification of diffusion parameters.

3.1.2. $Al_xGa_{1-x}As$/GaAs Heterostructures.

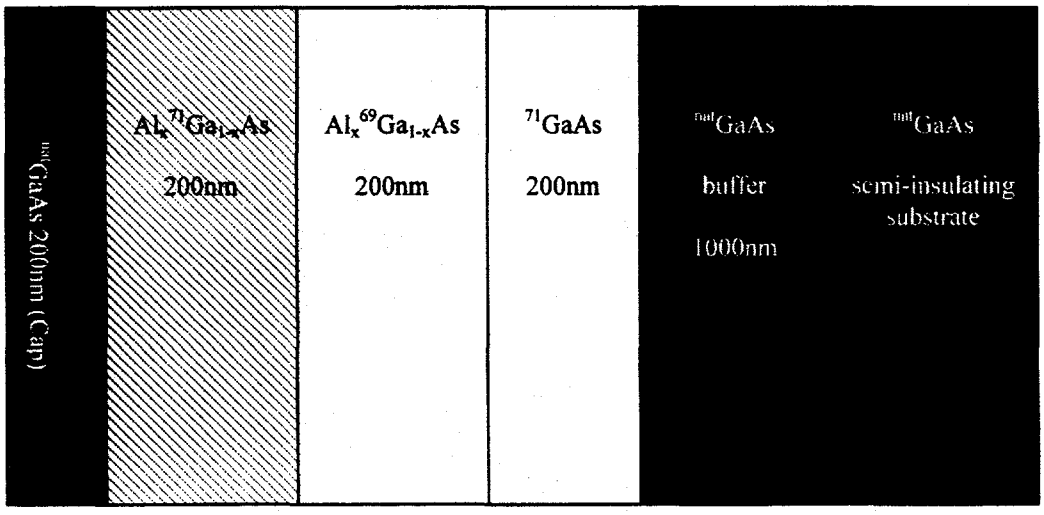

Figure 3-2: Schematic of AlGaAs isotope superlattice structures used in this work

The $Al_xGa_{1-x}As$/GaAs heterostructures (henceforth referred to generally as "AlGaAs samples") consisted of three layers of different aluminum concentrations and

gallium isotope enrichment, all grown on a semi-insulating substrate. On top of a 1000 nm ^{nat}GaAs buffer layer, a 200 nm thick layer of ^{71}GaAs was grown, followed by 200nm of $Al_x{}^{69}$GaAs, 200nm of $Al_x{}^{71}$GaAs and finally a 200nm ^{nat}GaAs cap layer. Three sets of identically layered samples were grown with silicon doping, Beryllium doping and with no extrinsic doping to examine the effect of doping on Ga diffusion. To delineate the contributions of each group III species to the AlAs/GaAs interdiffusion, four aluminum concentration variations of each of the three doping concentrations were grown for a total of 12 unique AlGaAs isotopically enriched heterostructures.

3.2. Sample Processing.

Central to all of the experiments performed was the closed ampoule diffusion technique discussed earlier. For these experiments 14 cm long quartz ampoules with an inner diameter of 1cm were used in conjunction with small quartz plugs with a 0.9 cm outer diameter. The ampoules and plugs where cleaned with acetone and then etched for 10-15 minutes with 13M hydrofluoric acid to remove any contaminants on the quartz surface. After cleaning and prior to sealing, the ampoules to be used for the superlattice samples were pre-annealed at the upcoming sample annealing temperature and then cooled in a N_2 ambient for 1-3 hours to remove any water adhering to the inner quartz walls. Palfrey, et al. (1981) found this to be essential for obtaining reproducible results. We observed qualitatively that there was a greater likelihood of the samples to remain specular if the ampoule was pre-annealed. In parallel with the ampoule cleaning, the samples and the GaAs substrate were cleaned in xylenes, acetone and methanol to remove any organic contamination before being rinsed with DI water and then etched in

concentrated HCl for < 1 minute to remove any surface oxide present. The samples and GaAs substrate were rinsed again in DI, rinsed with methanol and dried on a hot plate using a stream of N_2. Finally, the samples and the necessary diffusion sources were placed in the ampoule separated by the piece of SI GaAs. The ampoule was then attached to a small turbo pump, purged with ultra pure (99.9995%) Argon and then evacuated to approximately $1x10^{-5}$ torr. Finally the ampoule and plug were fused together using an H_2+O_2 torch creating a sealed vacuum compartment in the end of the ampoule for the annealing.

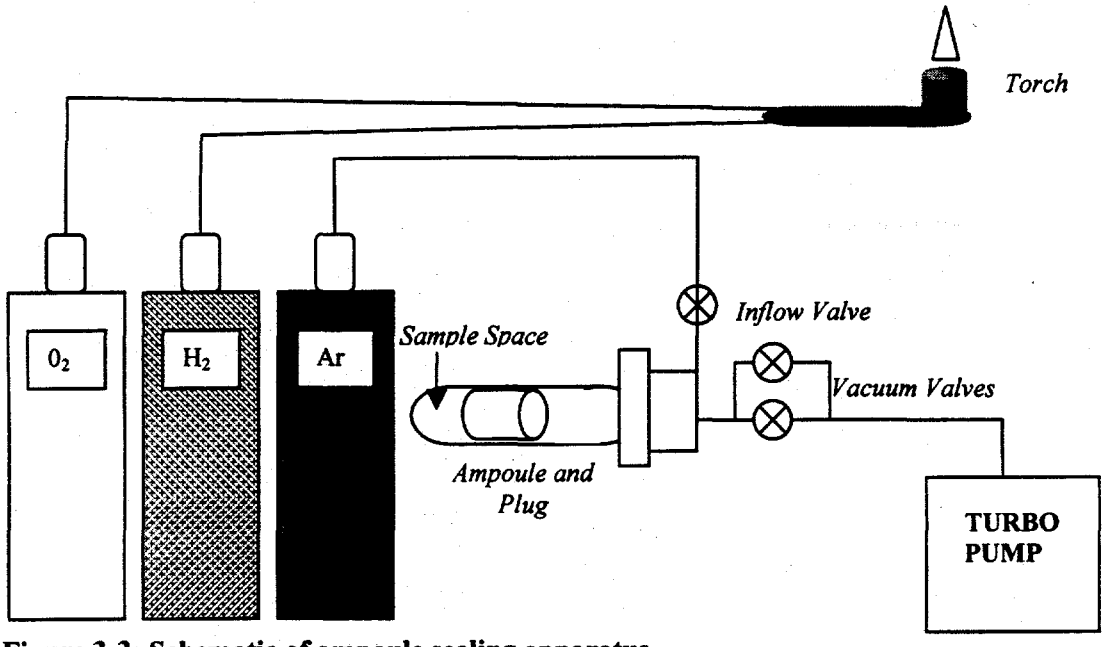

Figure 3-3: Schematic of ampoule sealing apparatus

The annealing runs of all the samples were performed in a highly thermally insulated resistance heated tube furnace. The annealing temperatures were determined using a type S thermocouple (TC) placed next to the samples inside the tube. The TC and sample were in indirect contact through opposite sides of a 1mm thick protective quartz TC housing so time for the ampoule to equilibrate to the furnace temperature could be

recorded. The thermocouple used had been previously calibrated between 500°C-1100°C and certified to deviate from the Type S TC reference table by less than 0.5°C (0.005mV). This standard error lies within the 2°C variation that our electronics and furnace controller were capable of measuring. Samples were removed from the furnace and quenched in ethylene glycol to arrest diffusion at the desired time. Ampoules that contained excess As were first cooled with water at one end to condense the As on the ampoule instead of on the samples before quenching in the glycol.

3.2.1. AlGaAs/GaAs Annealing Conditions.

Since the atomic movement of interest in these samples is located in the as-grown structure at buried interfaces, the annealing process needed to conserve the specular surface and purity of the samples. Any surface roughness will be preserved in the sputtering of the SIMS crater and introduces large errors in the concentration profiles and calculated diffusion coefficients. The samples were buried in undoped GaAs powder and annealed with enough solid As to produce a 1 atm As_4 overpressure. The GaAs powder was added to getter any ionic impurities, residual H_2O or solvents remaining in the quartz ampoule after cleaning as well as to keep the sample surrounded by GaAs to prevent surface degradation. The excess As was required to prevent decomposition of the GaAs powder at these elevated diffusion temperatures.

3.2.2. Zn Diffusion into GaAs Conditions.

Initially a diluted GaAs:Zn powder source such as that used by Bösker, et al. (1995) was attempted. GaAs powder was saturated with Zn at ~1250°C for >12 hours,

diluted with various ratios of undoped GaAs powder, annealed again to homogenize the dilute GaAs:Zn powder and then used as a diffusion source. Small quantities (50-100 mg) of this powder were placed in the ampoule with a small amount of solid arsenic to create a known overpressure of As_4. However, these dilute powdered alloys were not suitable for our experiments because the Zinc partial pressure of such sources was too low for the temperatures we were interested in studying.

Whereas Bösker used such diffusion sources at >900°C, we were interested in temperatures <700°C. Our choice of temperature range was based on two considerations. First, it was desirable for the Zn not to diffuse entirely through the 1μm structure such that diffusion effects in both the Zn affected and unaffected regions could be measured within the same sample, thus limiting the number of samples required and reducing the experimental error. Theoretically, suitable diffusion depths could be obtained at higher temperatures but the time required for such diffusions is less than the time required for the ampoule to equilibrate to the furnace temperature. Second, because the samples were to be modeled under Ga-rich conditions, lower diffusion temperatures were beneficial. Lower temperatures resulted in a lower partial pressure of As_x over GaAs and one which was near the Ga partial pressure so excess As wasn't needed in the ampoule to prevent incongruous evaporation.

To produce appropriate and repeatable Zn partial pressures at such temperatures alloys of Ga and Zn were used as diffusion sources. As described by Kendall and Banning (1977), such solid solutions can easily be used to moderate the Zn partial pressure and hence the amount of Zn arriving at the sample surface.

3.3. Alloy Preparation.

For the diffusion of Zinc into GaAs, a solid solution alloy was used because it provided the most practical means of creating a well defined and reproducible Zinc overpressure which would result in the desired Zinc surface concentration 2-20 times below the GaAs:Zn saturation level. All alloys were prepared using 7N (99.99999%) pure gallium or 6N pure indium and 6N pure zinc. The desired ratio of materials was added to an etched quartz ampoule that was purged and sealed. Prior to sealing, the ampoules were filled with enough argon to create ~0.5 atm of overpressure at the homogenization temperature to improve heat conduction from the ampoule during quenching. The sealed ampoules were placed in a vertically mounted resistance heated furnace at 550°C for 4-20 hours to homogenize the alloys. In order to limit phase separation during cooling of the homogenous liquid alloy, the ampoule was dropped from the furnace immediately into a large ethylene glycol bath below. After removal from the ampoule, the alloys were refrigerated until needed since the eutectic temperature of utilized alloy systems are very near room temperature.

3.4. Characterization.

3.4.1. Electrochemical C-V (ECV)

One of the key characterization techniques for these studies was electrochemical C-V profiling to determine the active concentration of majority carriers in the samples after annealing. The specifics of the electrochemical C-V profiling are described in Appendix 1. Basically, the ECV produces a profile of the electrically active carrier

concentration versus depth within a sample. By assuming that the vast majority of injected carriers are the desired diffused/doped impurity atoms, the ECV provides a low cost method for approximating dopant impurity diffusion profiles by determining the concentration of dopants over a theoretically unlimited depth into the sample. Coupled with calibrated SIMS profiles of the expected dopant, ECV provides a good measure of the concentration of electrically active dopants which is a critical parameter for determining the contributions of various diffusion processes mediated by the Fermi level. If the ECV and SIMS profile shapes correlate and other dopant species that could possibly be introduced (i.e., C and O) are not detected by SIMS, the dual quantification can improve overall accuracy with which the impurity concentration profile is known.

All samples were measured using a Bio Rad PN4300 Series ECV profiler with a ~0.01cm^2 diameter sealing ring. AlGaAs samples were etched using 0.1M Tiron as the electrolyte while for GaAs:Zn samples Tiron or NaOH:EDTA was used. Calibration and correction of the ECV profiles was achieved using three post-etch measurements. The depth of the etched hole was measured using a Dektak Model IIA profilometer which is capable of determining depth to within 50 nm to check against the etch depth calculated by the ECV by measuring the current during etching. Ideally, any difference between the calculated and measured depths should be corrected for redundantly by differences between the initial area approximation and the measurement of the actual etched area after the etching is complete. An optical microscope was used to measure the diameter of the etched hole. As a final calibration, bulk GaAs:Si and GaAs:Zn were regularly profiled to depths similar to those of the actual samples. These particular commercial samples were chosen because they had an active impurity concentration of the same magnitude as

the experimental samples. The exact impurity concentration in some of the bulk samples was determined using Hall effect measurements which have a much better accuracy than the ECV. After the aforementioned depth and area corrections of the bulk calibration samples, any discrepancies between the Hall Effect results and the steady state concentration measured by the ECV determine the ECV repeatability and any measurement correction factors. It is important to note that while ECV and SIMS measurements for the n-type AlGaAs samples were performed on the exact same sample, the limited amount of GaAsSL2 material made this prohibitive for the superlattice samples because of the minimum sample size needed to perform ECV. SIMS samples of 1 x 3-4 mm^2 were prepared while the ECV requires a minimum sample dimension of 2 x 4-5mm^2. Alternatively, ECV measurements were made using the SI GaAs wafer piece that was included in the ampoule with the sample and diffusion source.

Also, we were unable to measure any of the annealed p-type AlGaAs samples with the ECV. Attempts with a variety of electrolytes resulted in extremely non-uniform etching of the sample surface. Since it was possible to measure the as-grown structures, it seems likely that some sort of nonconductive film (BeO?) or chemical reaction transforms the sample surface during annealing. Similar observations have been made by at least one other group and we could find no reports of ECV measurements of annealed AlGaAs:Be in the literature.

3.4.2. Secondary Ion Mass Spectroscopy (SIMS)

After removal from the ampoule, the samples were again cleaned briefly with solvents. To provide easier handling and assure accurate mounting of the samples in the

SIMS apparatus, these small samples were mounted in germanium holders using a silver (Ag) emulsion paint. The holders consisted of a 6x6x6 mm^3 cube cut from a Ge ingot with an inner diameter (ID) circular diamond saw with a groove cut into the holders to a depth equal to the samples thickness. Care was taken to ensure that cuts creating the holder and groove sides were perpendicular to all adjoining sides.

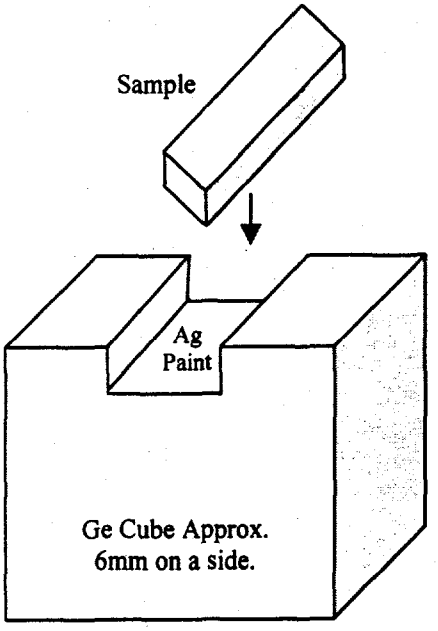

Figure 3-4: Sample mounting setup for SIMS

Although the SIMS apparatus holder in which the Ge mounted samples were placed should keep the sample surface perpendicular to the incident beam, non-uniform holder groves could affect the accuracy of the SIMS profile. The Ag emulsion was used both as an easily soluble adhesive and as a conductive interface to channel any charging effect caused by the ion beam to the grounded apparatus holder.

After mounting, samples were taken to a commercial analysis service for SIMS measurements. Samples for this work were profiled at either Charles Evans & Associates in Redwood City, CA (all AlGaAs samples) or the Materials Analysis Group in

Sunnyvale, CA (GaAs SL samples). At both facilities a Cameca 3F or 4F instrument was used and the samples were sputtered with a Cs+ beam. A 14.5keV beam was used for AlGaAs:Si sputtering and from sputtering the GaAs:Zn samples ion energies of 0.5-3 keV were used. Calibration standards were used to quantify the impurity concentrations and sputter rate measurements were performed on the AlGaAs samples to correct for differences between the GaAs and AlAs sputter rates. A more detailed description of the SIMS technique can be found in Appendix A.

3.5. Diffusion Profile Simulation and Fitting

3.5.1. Ga Diffusion at ^{71}GaAs/^{nat}GaAs Interface of AlGaAs Samples

The ^{69}Ga diffusion profiles across the ^{71}GaAs/ ^{nat}GaAs interface were fitted to the solution of Ficks's law for self-diffusion across an interface allowing for the possible contribution of ^{69}Ga from the preceding Al^{69}GaAs layer by Dr. Bracht. The solution for this system can be written as

$$C_{^{69}Ga} = \frac{C_1 + C_3}{2} + \frac{C_2 - C_1}{2} erf\left(\frac{x - x_1}{2\sqrt{D_{Ga}t}}\right) + \frac{C_3 - C_2}{2} erf\left(\frac{x - x_2}{2\sqrt{D_{Ga}t}}\right) \qquad (3.1)$$

(Crank 1975) Where C_1, C_2, C_3 are the ^{69}Ga concentrations in the Al^{69}GaAs, ^{71}GaAs, and ^{nat}GaAs layers respectively, x_1, x_2 are the depths of the Al^{69}GaAs/^{71}GaAs and ^{71}GaAs/ ^{nat}GaAs interfaces and t is the diffusion time. The Ga isotope concentrations were taken from the SIMS measurements and a best fit was found for the ^{69}Ga diffusion profile by optimizing D_{Ga}, x_1, and x_2. Optimizing the interface depths allows for accounting of any possible depth inaccuracies in the SIMS measurement and does not significantly alter the shape of the modeled diffusion profile or best-fit value of D_{Ga}.

3.5.2. Zn diffusion in GaAs superlattice structures

The final GaAs:Zn superlattice profiles were modeled by Dr. Hartmut Bracht using the ZOMBIE software package running on a VAX computer. ZOMBIE can solve numerically a series of coupled partial differential equations, such as those that describe our diffusion experiments. The SIMS profiles of a given species in the as-grown and post-annealed structures were used to determine the depth distribution and concentration of atoms, while the ECV profiles were used to determine the net dopant concentration profiles.

The boundary conditions for Zn CPDE diffusion equations describe the assumption of equilibrium intrinsic conditions at the surface.

$$\tilde{C}_{s,i,I}(x=0,t)=1 \tag{3.2}$$

The initial conditions assume local equilibrium in the sample during the diffusion. The first condition is that the Ga self-interstitial concentration is uniform and at its equilibrium level at the beginning of the diffusion process.

$$C_I(x,t=0)=C_I^{eq}(\text{intrinsic}) \tag{3.3}$$

This means according to [2.15] that

$$\tilde{C}_I(x,0)\approx\tilde{n}_i^2 \tag{3.4}.$$

Depending on the temperature and Zn surface concentration equation 3.4 gives $\tilde{C}_I(x,0)$~0.001^2-0.005^2 in our experiments but this value causes convergence problems for the ZOMBIE software so a value of 0.01^2 was used. This assumption was verified to not significantly affect the shape of the simulated profiles. From the reaction [2.13] local equilibrium dictates that

$$\tilde{C}_i - \tilde{C}_s \tilde{C}_I = 0 \quad \text{at } t = 0 \tag{3.5}$$

Assuming

$$\tilde{C}_s(x,0) = 10^{-4} \tag{3.6}$$

the remaining initial concentration is then

$$\tilde{C}_i(x,0) = 10^{-4} * \tilde{n}_i^2 = 10^{-8} \tag{3.7}$$

The first boundary condition for the Ga diffusion is

$$\tilde{C}_{Ga}^{69/71}(0,t) = 0.5 \tag{3.8}$$

since the Ga isotope layers are of equal thickness, the completely homogenous superlattice will have a Ga lattice occupied by Ga^{69} and Ga^{71} in equal proportions. The first initial condition is

$$\left.\frac{\partial \tilde{C}_{Ga}^{69/71}}{\partial x}\right|_{x=d} = 0 \tag{3.9}$$

since there is no concentration gradient in the Ga isotope profiles. Only discontinuous steps exist between isotope layers which are differently isotopically enriched. The second initial conditions is

$$\tilde{C}_{Ga}^{69/71}(x,0) \approx \text{As} - \text{grown } Ga^{69/71} \text{ profile} \tag{3.10}$$

Using the above conditions, simulations were run to find the best fit values of the effective Zn and Ga interstitial diffusivity. Since the annealing runs were performed under As poor conditions the I_{Ga} diffusivity was normalized to As_4=1atm using Arthur's (Arthur 1965) measured As partial pressures. The temperature dependence of As_4 pressures from his work can be fitted to

$$P_{As_4} = 8.0 * 10^{16} \exp\frac{-5.44eV}{kT} \tag{3.11}$$

4. Results

4.1. Carrier Concentration Measurements in AlGaAs Samples

The following profiles were obtained for the net-dopant concentration (again assumed to be equal to the free carrier concentration) in doped AlGaAs before and after annealing. All ECV profiles are superimposed on the SIMS profile of the corresponding sample. For the as grown structures the samples with the lowest Al concentration produced the most accurate profiles and are shown immediately below.

After adjusting the SIMS and ECV profiles based on the local Al concentration the ECV plot seen in figure 4-1 of the as-grown n-doped AlGaAs sample was obtained. The profile of the free carriers in the lowest Al concentration sample doped with Be is seen in figure 4-2.

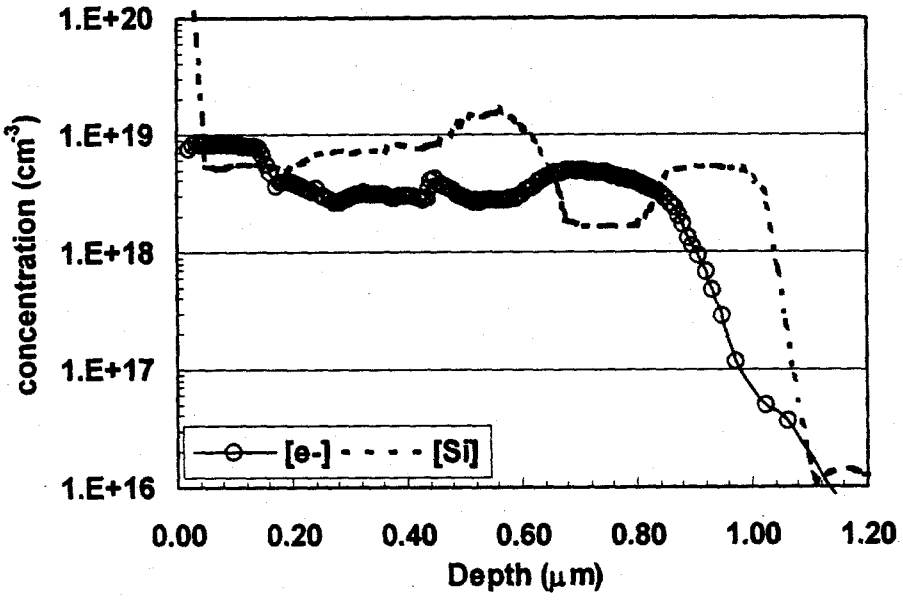

Figures 4-1: SIMS and ECV profiles of Sample 2a (AlGaAs:Si) prior to annealing

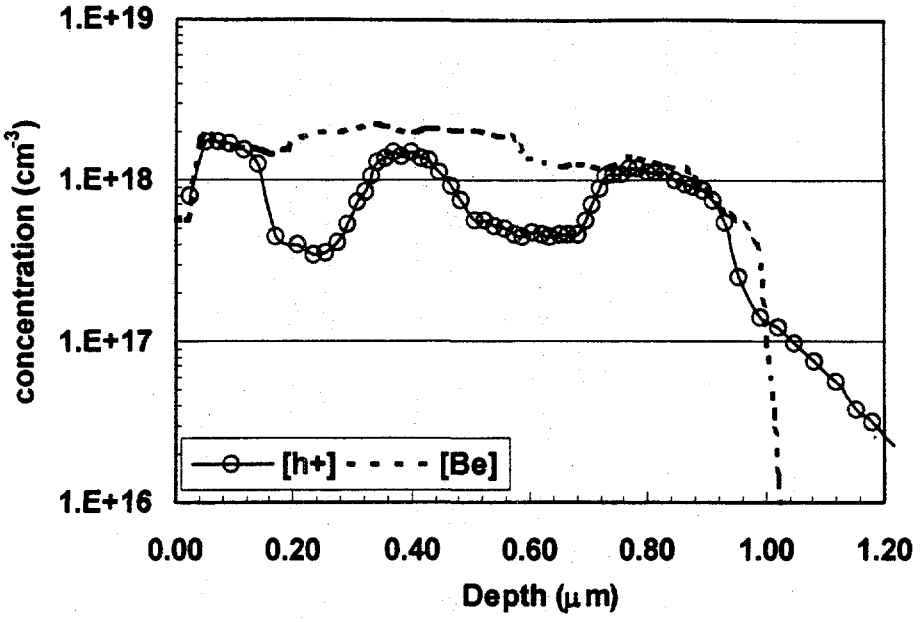

Figures 4-2: SIMS and ECV profiles of Sample 3a (AlGaAs:Be) prior to annealing

As mentioned previously attempts to profile the annealed AlGaAs:Be samples were unsuccessful but it was possible to measure the profile of annealed AlGaAs:Si on a number of structures which were large enough and had a suitable post annealing surface quality. In the following figures and tables the samples are designated by doping type, Al content and diffusion sequence such as 2a-1 where "2" denotes Si doping (3= Be doping), "a" denote Al content (a=0.41, b=0.62, c=0.68, d=1.0), and "-1 " simply denotes the order of annealing experiments and the time and temperature of the annealing.

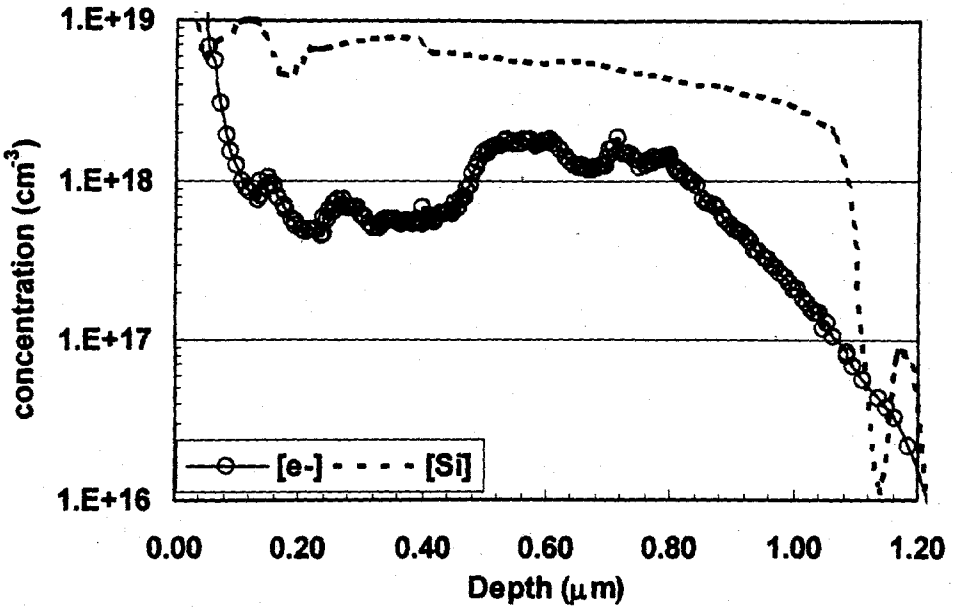

Figures 4-3: SIMS and ECV profiles of Sample 2b after annealing at 736° for 8.5 hours

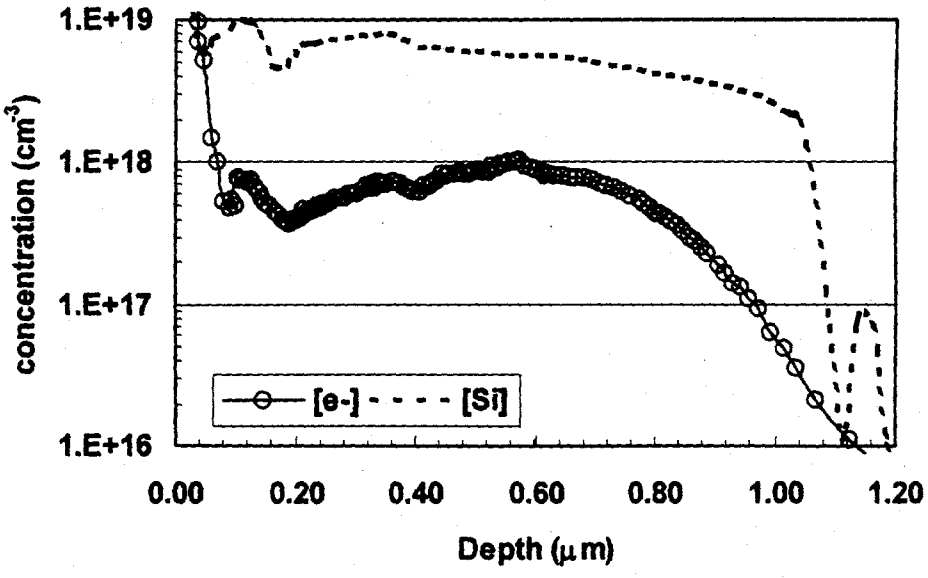

Figures 4-4: SIMS and ECV profiles of Sample 2c after annealing at 736°C for 8.5 hours

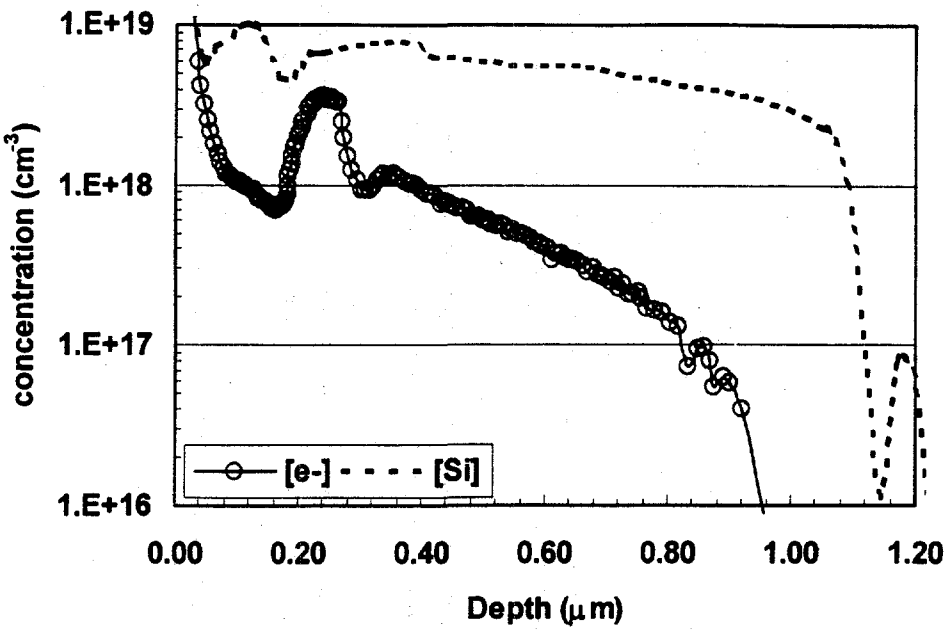

Figures 4-5: SIMS and ECV profiles of Sample 2d after annealing at 736°C for 8.5 hours

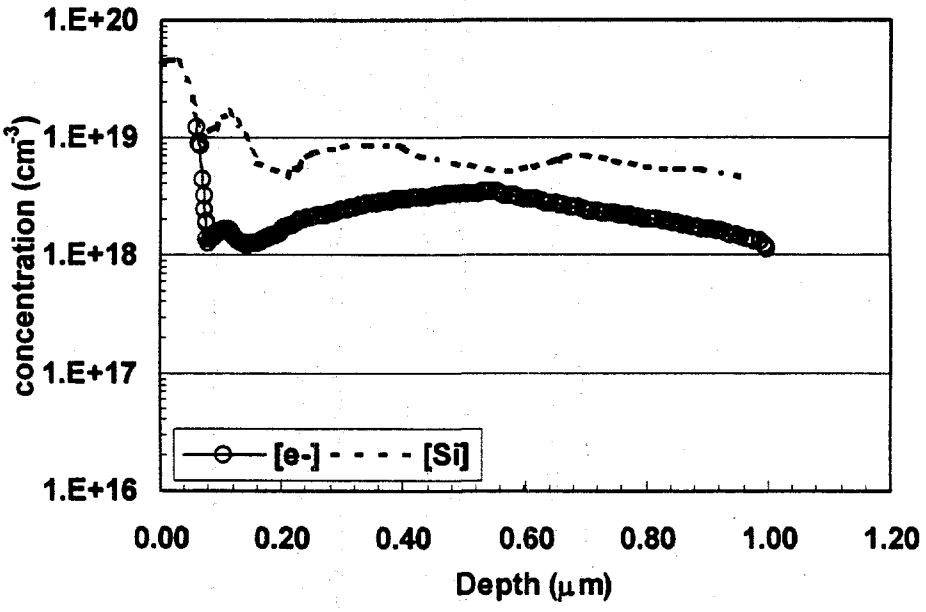

Figures 4-6: SIMS and ECV profiles of Sample 2a after annealing at 800°C for 2 hours

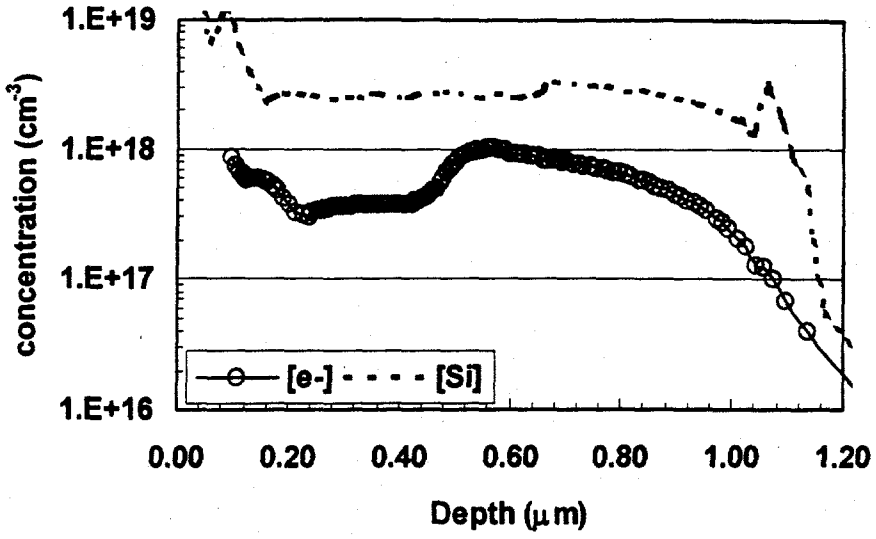

Figures 4-7: SIMS and ECV profiles of Sample 2b after annealing at 800°C for 2 hours

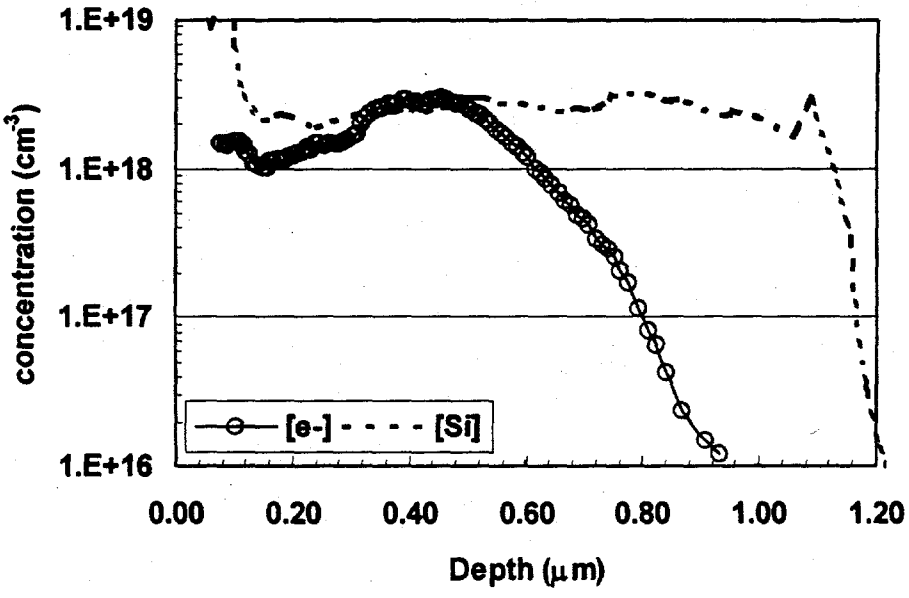

Figures 4-8: SIMS and ECV profiles of Sample 2c after annealing at 800° for 2 hours

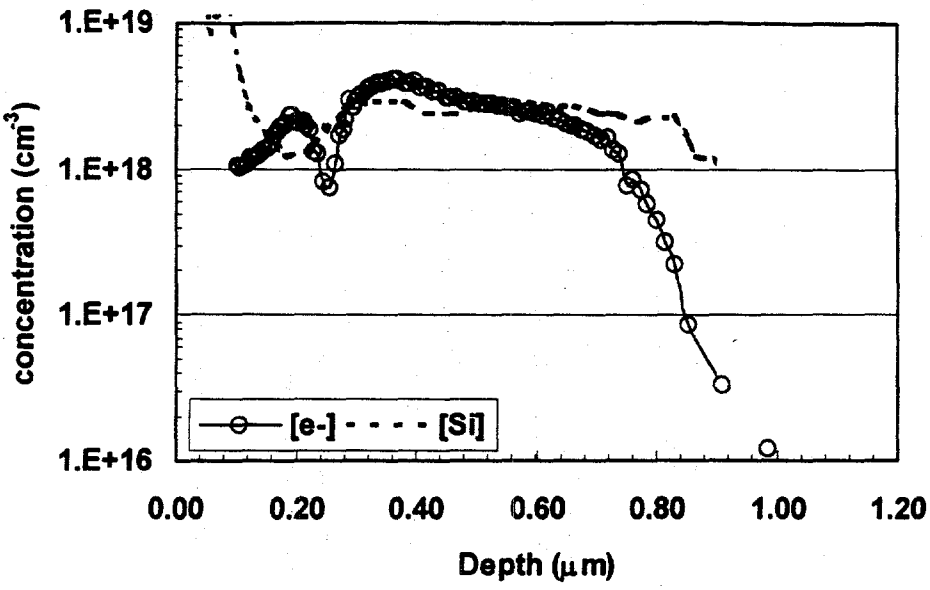

Figures 4-9: SIMS and ECV profiles of Sample 2d after annealing at 800°C for 2 hours

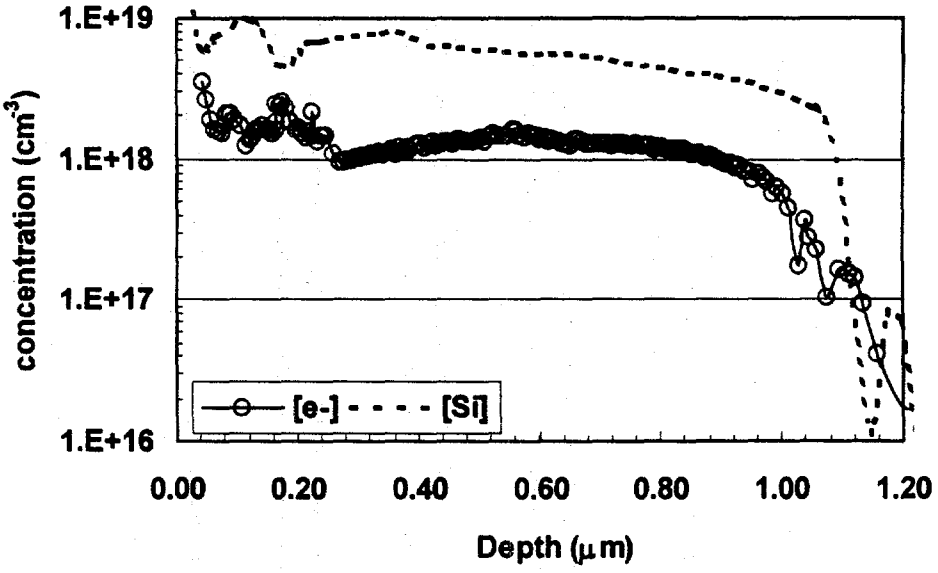

Figures 4-10: SIMS and ECV profiles of Sample 2a after annealing at 872° for 28 minutes

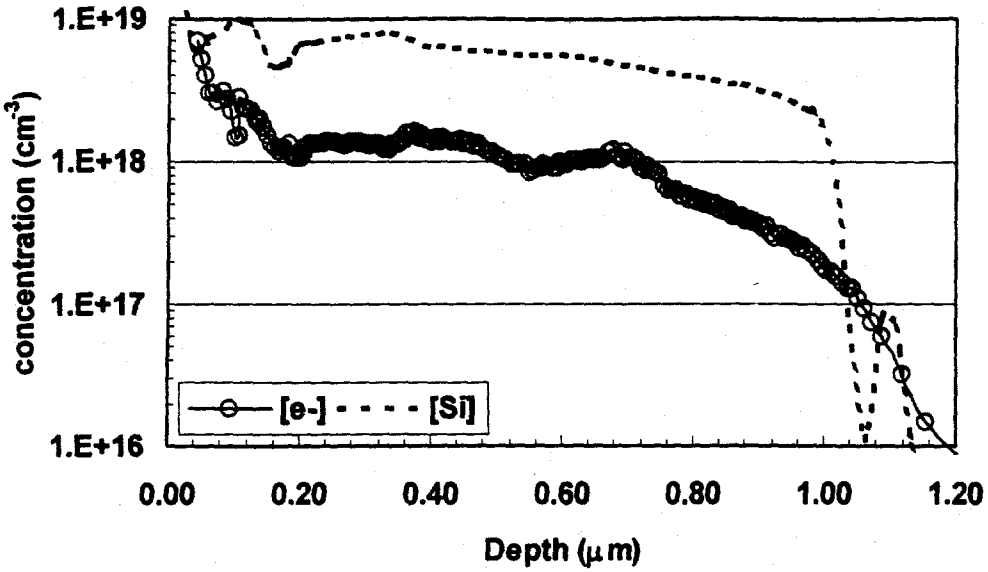

Figures 4-11: SIMS and ECV profiles of Sample 2c after annealing at 872° for 28 minutes

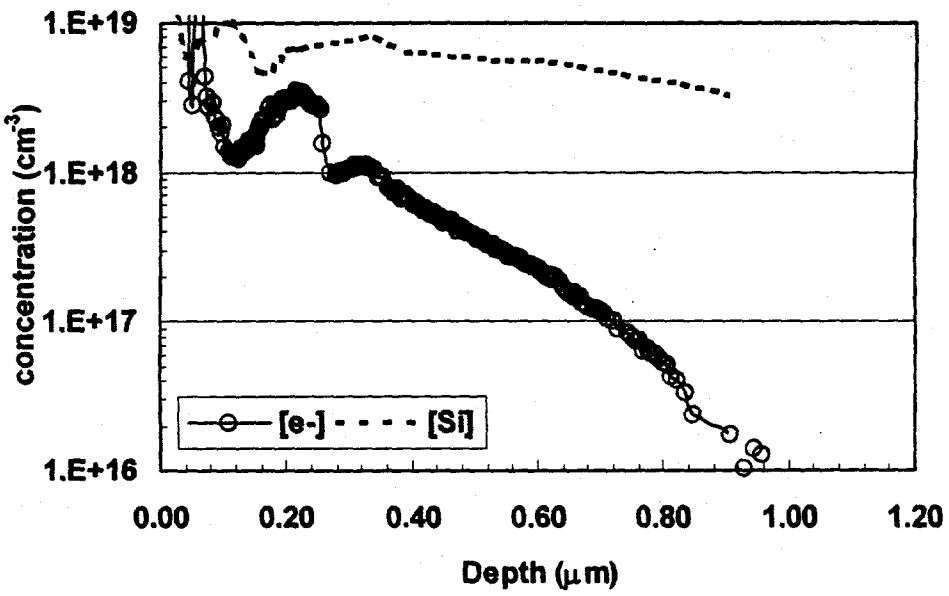

Figures 4-12: SIMS and ECV profiles of Sample 2d after annealing at 872°C for 28 minutes

To investigate the difference between the SIMS and ECV profiles a comparison was made between the total charge measured in the ECV plots relative to Hall Effect

measurements of the as-grown sample structures using the correction factor from ECV calibration runs done with bulk samples.

Table 4-1: Comparison of sample doping measured by ECV and Hall Effect by the growers (MPI) and this author (LBNL)

		ECV	Hall Effect*		HE/ECV
	Sample	**Integrated Dose (q^*cm^{-2})**	**Location**	**Dose (q^*cm^{-2})**	**(uncorrected)**
As-grown	GaAs:Si Bulk♦	1.12E+14	LBNL	1.74E+14	***1.55***
	GaAs:Zn Bulk♦	1.22E+14	LBNL	1.95E+14	1.60
	2a	2.83E+14	LBNL	3.14E+14	1.11
		2.83E+14	MPI	6.08E+14	2.15
	3a	8.60E+13	LBNL	8.55E+13	0.99
		8.60E+13	MPI	1.80E+14	2.09
Annealed	2a-1(800°C, 2 hrs)	1.91E+14	LBNL	3.14E+14	1.06[1] (1.64)
	2a-1(800°C, 2 hrs)	1.91E+14	MPI	6.08E+14	2.05[1] (3.18)
	2a-2(872°C, 28 min)	9.33E+13	LBNL	3.14E+14	2.17[1] (3.36)
	2a-2(872°C, 28 min)	9.33E+13	MPI	6.08E+14	4-20[1] (6.52)
	2b-6(736°C, 8.5 hrs)	1.49E+14	MPI	3.14E+14	1.36[1] (2.10)
	2c-1(800°C, 2 hrs)	7.91E+13	MPI	2.66E+14	2.17[1] (3.36)
	2c-2(872°C, 28 min)	9.20E+13	MPI	2.66E+14	1.87[1] (2.89)
	2c-3(736°C, 8.5 hrs)	1.41E+14	MPI	2.66E+14	1.22[1] (1.89)
	2d-1(800°C, 2 hrs)	1.11E+14	MPI	2.56E+14	1.49[1] (2.30)
	2d-1(800°C, 2 hrs)	1.45E+14		2.56E+14	1.14[1] (1.77)
	2d-2(872°C, 28 min)	2.41E+14	MPI	2.56E+14	0.69[1] (1.06)
	2d-3(736°C, 8.5 hrs)	8.93E+13	MPI	2.56E+14	1.85[1] (2.87)

♦ Average of all calibration runs

* Due to the limited amount of material available for diffusion studies and sample size requirements, all Hall Effect measurements were possible on as-grown material only.

[1] Corrected by multiplying the raw ECV integrated charge by ***1.55.***

4.2. Zn In-diffusion Induced Disordering of $^{69}GaAs/^{71}GaAs$ Superlattics

The first attempt to produce IILD was made with the superlattice structure that had different growth temperatures (GaAsSL1) for proof that the dilute alloy technique would work. This experiment was done with an In-Zn source because the higher In-Zn eutectic temperature (143.5°C) made the alloy solidification and storage easier.

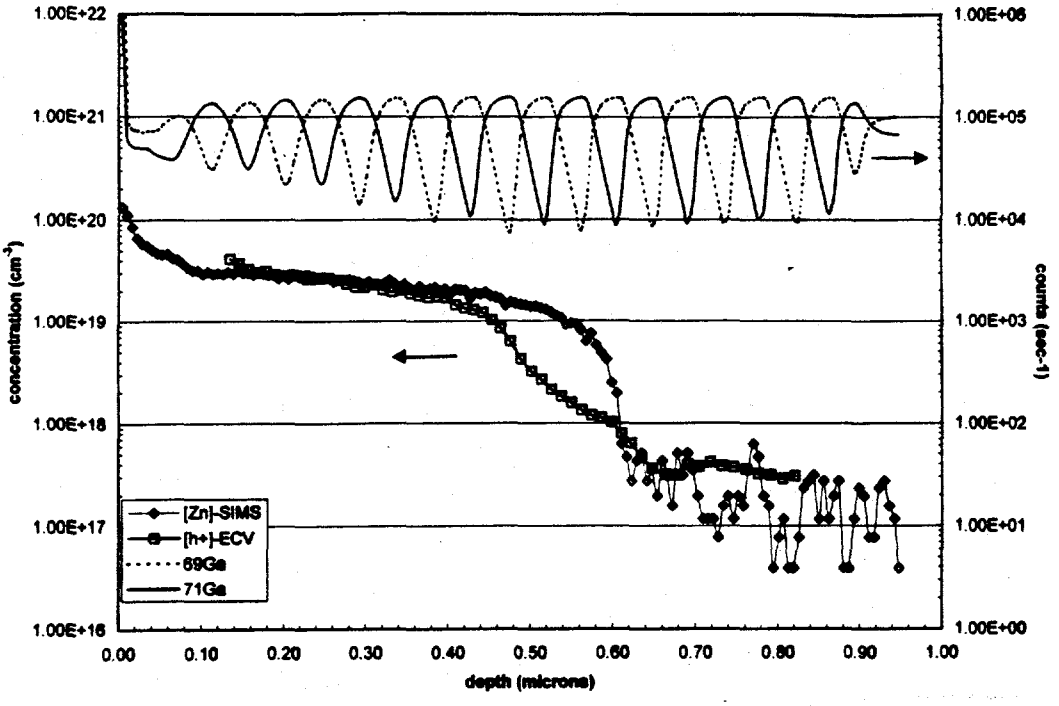

Figure 4-13: SIMS profile of GaAsSL1 after annealing at 616°C for 25 minutes with a In-Zn (10%) source

After this experiment was successful, similar, but operationally more difficult, Ga-Zn alloys (T_e=24-7°C) were used as the diffusion sources for annealing with pieces of the GaAsSL2 samples. Even though the partial pressure of In is extremely small, the Ga-Zn source was made to limit all possible surface contamination. Samples were annealed at three different temperatures (618°C, 666°C, and 714°C) with two different alloy sources (Zn=10% and 20%) for time periods that were estimated to place the Zn diffusion front in the middle section of the superlattice structure. This location was chosen so there would possibly be both IILD near the surface and there would also be parts of the structure that were free of any Zn effects. Disordering of these later periods would be

solely due to intrinsic self-diffusion and thus intrinsic and extrinsic diffusion could be compared within the same sample.

SIMS and ECV profiles of the resultant sample are seen in figures 4-14-4-19. For clarity only Ga^{71} profiles are includes although profiles of ^{69}Ga were also recorded. Also included in the plots are the best fit (–fit) of the SIMS/ECV results to the simulation. Based on these results the calculated profiles of Ga and Zn interstitials (I_{Ga}-simulation and Zn_i-simulation) are also included. Zn_s-fit denotes the best fit to the three CPDE describing the Zn diffusion while Zn_s-sl-fit denotes the best fit to the five CPDE describing the GaAs superlattice disordering.

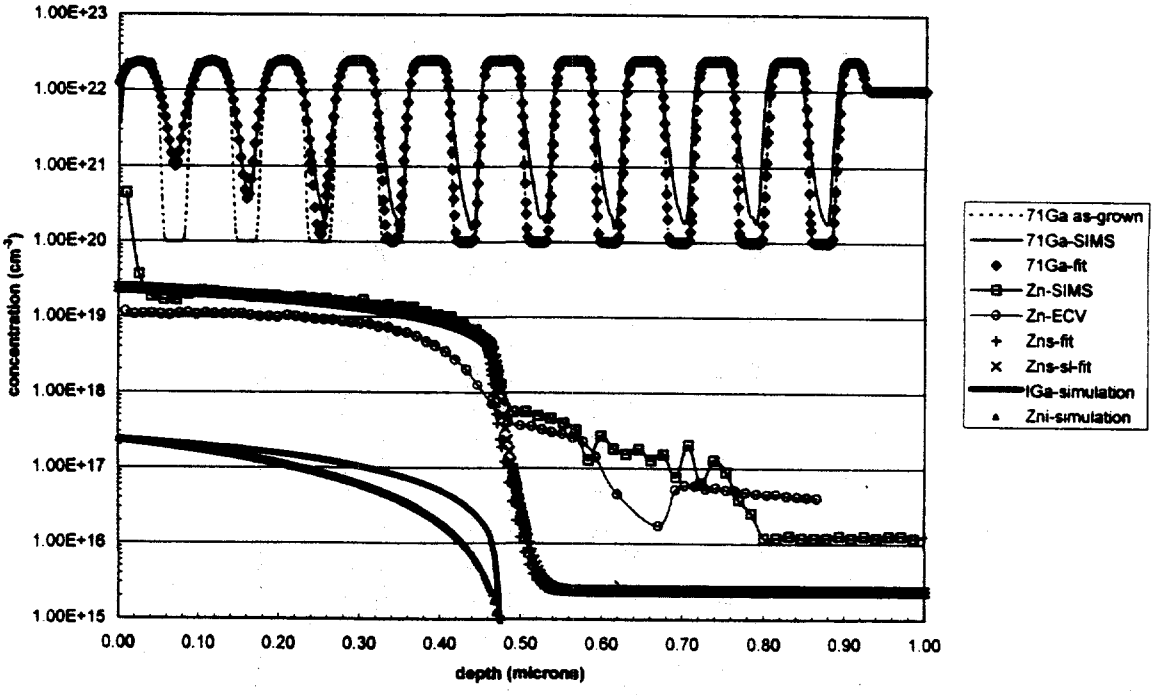

Figure 4-14: SIMS and ECV profiles of GaAsSL2 after annealing at 618°C for 25 minutes with a Ga-Zn (20%) source with predicted Ga interstitial (I_{Ga}) and Zn interstitial (Zn_i) concentration profiles also included

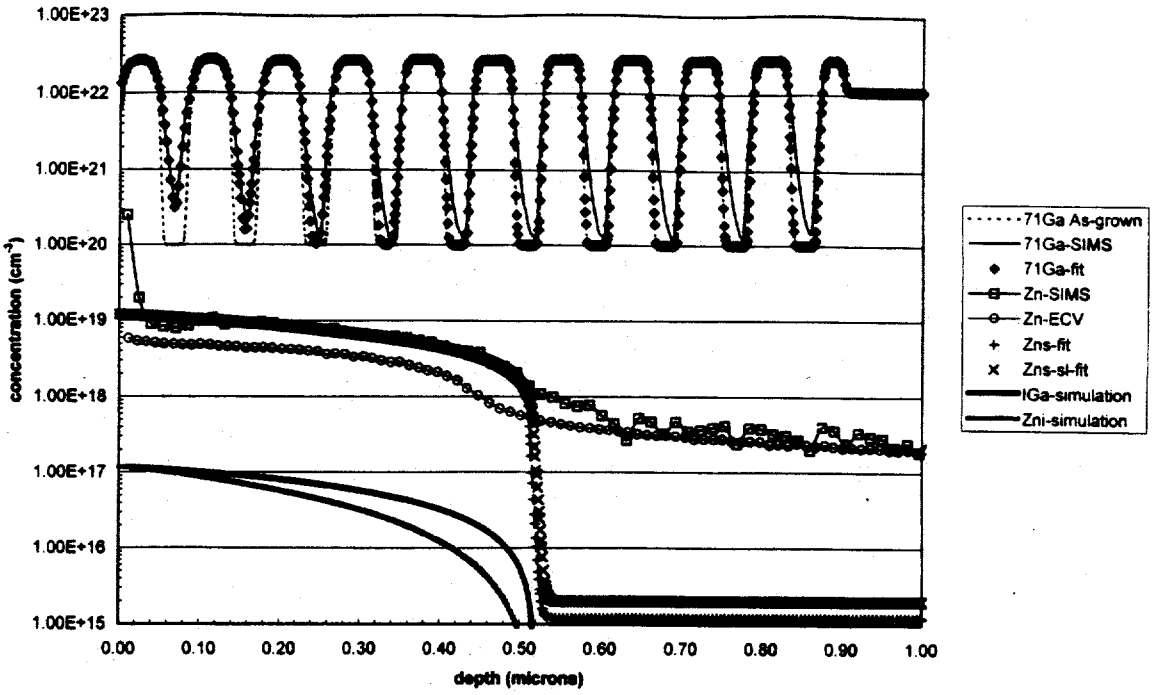

Figure 4-15: SIMS and ECV profiles of GaAsSL2 after annealing at 618°C for 300 minutes with a Ga-Zn (10%) source with predicted Ga interstitial (I_{Ga}) and Zn interstitial (Zn_i) concentration profiles also included

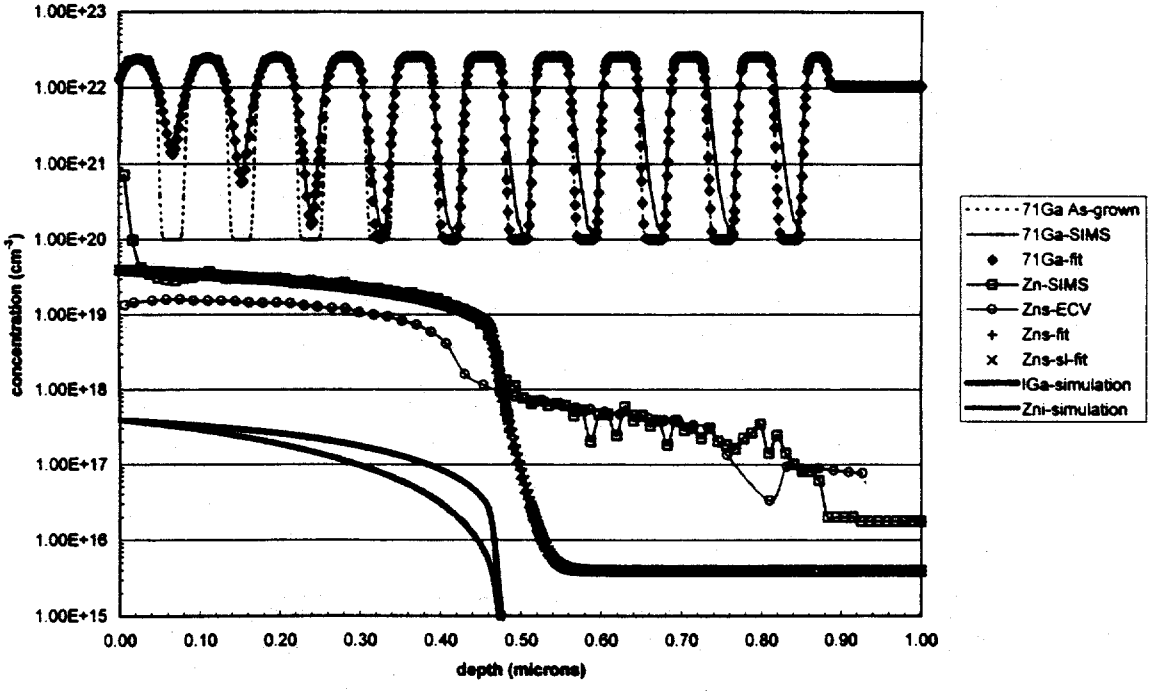

Figure 4-16: SIMS and ECV profiles of GaAsSL2 after annealing at 666°C for 15 minutes with a Ga-Zn (20%) source with predicted Ga interstitial (I_{Ga}) and Zn interstitial (Zn_i) concentration profiles also included

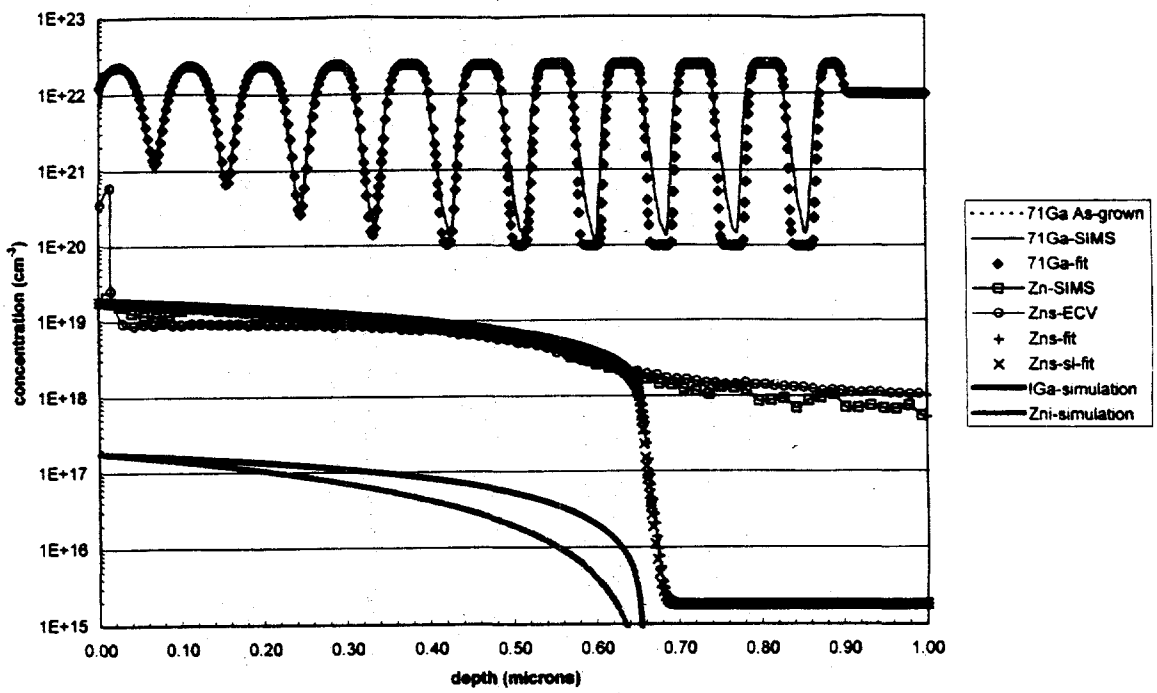

Figure 4-17: SIMS and ECV profiles of GaAsSL2 after annealing at 666°C for 180 minutes with a Ga-Zn (10%) source with predicted Ga interstitial (I_{Ga}) and Zn interstitial (Zn_i) concentration profiles also included

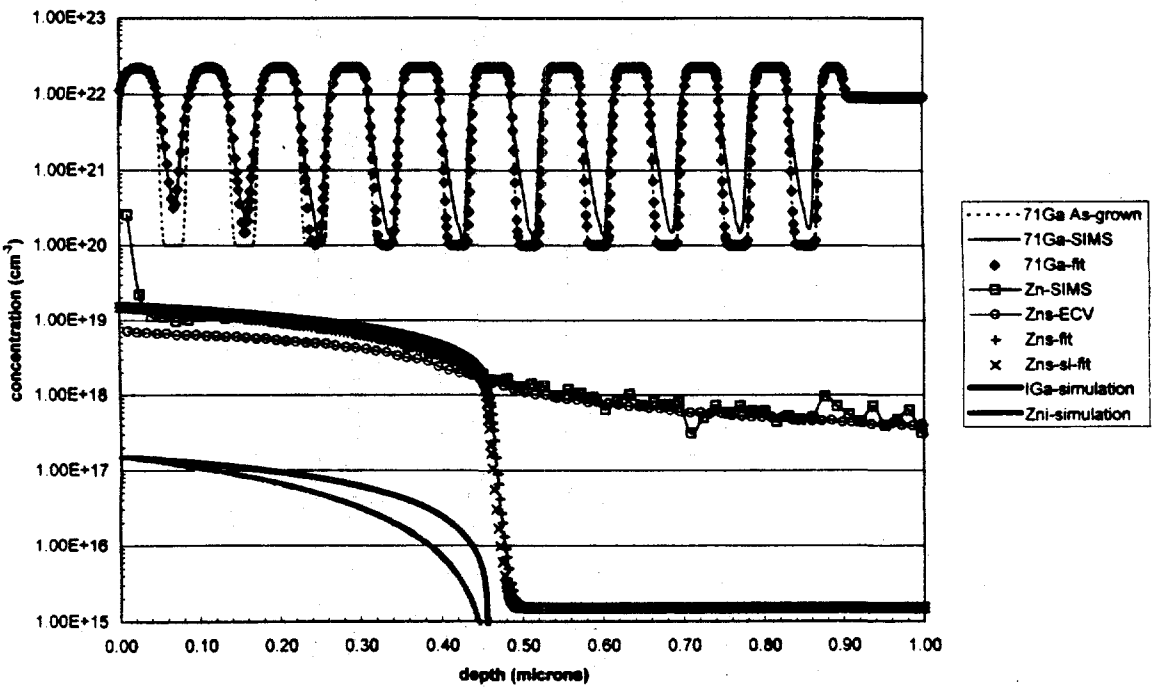

Figure 4-18: SIMS and ECV profiles of GaAsSL2 after annealing at 666°C for 90 minutes with a Ga-Zn (10%) source with predicted Ga interstitial (I_{Ga}) and Zn interstitial (Zn_i) concentration profiles also included

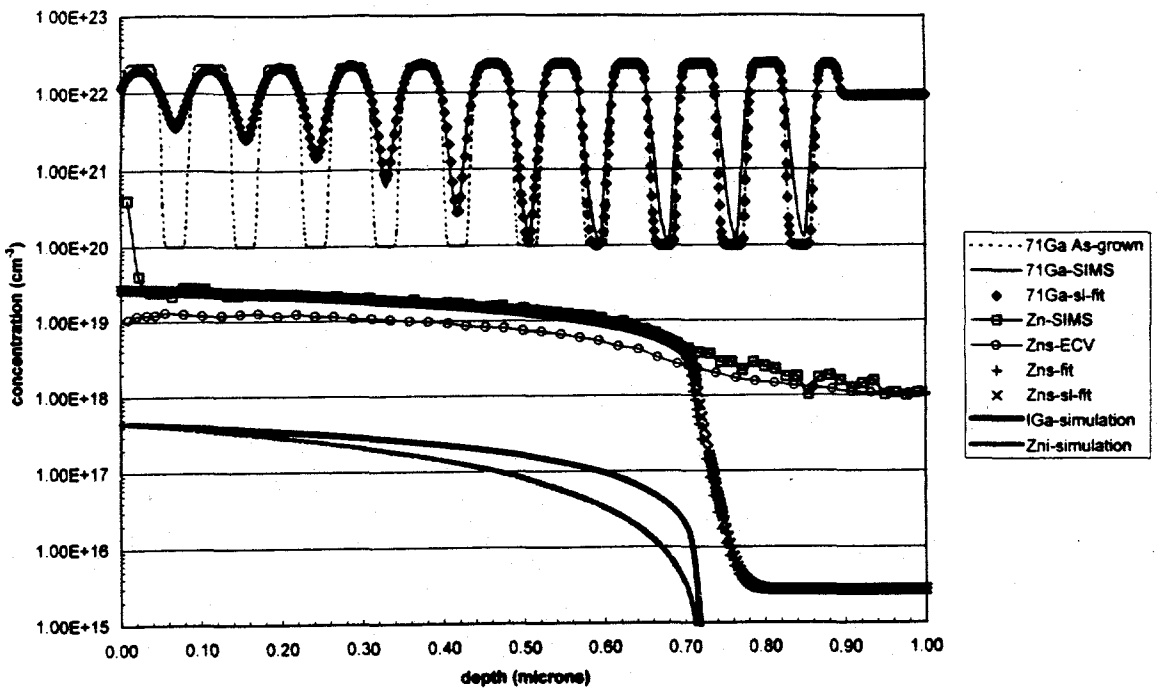

Figure 4-19: SIMS and ECV profiles of GaAsSL2 after annealing at 714°C for 45 minutes with a Ga-Zn (10%) source with predicted Ga interstitial (I_{Ga}) and Zn interstitial (Zn_i) concentration profiles also included

Built into these simulation fits are the extracted values for the effective diffusivity of the various Zn and Ga species. These extracted values are summarized in Table 4-2

Table 4-2: (a) Fitting input parameters and (b) extracted parameters

(a)

Sample	T [°C]	n_i [cm^{-3}]	p_{As} [atm]	p^{eq} [cm^{-3}]
616-25-20	616	8.60E+15	1.16E-14	1.6E+19
618-25-20	618	8.85E+15	1.36E-14	1.1E+19
618-300-10	618	8.85E+15	1.36E-14	5.0E+18
666-15-20	666	1.71E+16	5.08E-13	1.7E+19
666-90-10	666	1.71E+16	5.08E-13	7.0E+18
666-180-10	666	1.71E+16	5.08E-13	9.1E+18
714-15-20	714	3.15E+16	1.34E-11	3.0E+19
714-45-10	714	3.15E+16	1.34E-11	1.3E+19
714-120-10	714	3.15E+16	1.34E-11	6.8E+18

618-25-20	2.1E-12	2.0E-22	≥5.0E-11			
618-25-20	6.5E-13	1.4E-22	≥5.0E-12	1.8E-12	8.9E-16	2.0E-25
618-300-10	6.0E-14	6.4E-23	≈8.0E-14	8.8E-14	2.0E-17	2.1E-26
666-15-20	1.1E-12	9.4E-22	≈4.0E-12	2.0E-12	1.5E-15	1.3E-24
666-90-10	1.6E-13	8.1E-22	≈1.0E-13	2.3E-13	7.2E-17	3.6E-25
666-180-10	1.6E-13	4-8E-22	≈1.0E-13	1.4E-13	5.9E-17	1.8E-25
714-15-20	7.0E-12	1.5E-20	≥5.0E-11	9.4E-12	1.3E-14	2.7E-23
714-45-10	8.0E-13	9.7E-21	≈1.5E-12	1.7E-12	9.5E-16	1.2E-23
714-120-10	4-0E-13	1.6E-20	≥5.0E-13			

From fitting of the Zn diffusion model to the SIMS profiles the effective diffusivity of Ga interstitials, $D_{I_{Ga}}^{eff}$, and substitutional Zn, $D_{I_{Ga}}^{eff}$, were deduced where

$$D_s^{eff} = \frac{C_{Zn_i}^{eq} D_{Zn_i}}{C_{Zn_s}^{eq}} \tag{4-1}$$

and

$$D_{I_{Ga}}^{eff} = \frac{C_{Zn_i}^{eq} D_{Zn_i}}{C_{I_{Gas}}^{eq}} \tag{4-2}.$$

The Zn diffusivity normalized to intrinsic conditions (n=p=n_i and P=1atm) is given by

$$D_{s,r}^{eff} = D_s^{eff} \left(\frac{n_i}{p}\right)^2 \left(\frac{p_{As_4}}{1atm}\right)^{1/4} \tag{4-3}$$

From fitting of the disordered Ga profile the effective diffusivity of the Ga interstitials, $D_{I_{Ga}}^{eff}$ was deduced. From this, the Ga self-diffusion in the lattice $D_{I_{Ga}}^{SD}$ and intrinsic Ga interstitial diffusivity $D_{I_{Ga},r}^{eff}$ were calculated using

$$D_{I_{Ga}}^{SD} = D_{I_{Ga}}^{eff} \frac{p^{eq}}{2.22015e22} \tag{4-4}.$$

and

$$D_{I,r}^{eff} = D_I^{eff}\left(\frac{n_i}{p}\right)^2\left(\frac{p_{As_4}}{1atm}\right)^{1/4} \qquad (4\text{-}5)$$

5. Discussion

5.1. Enhanced Self-diffusion of Ga

Modeling of the AlGaAs diffusion profiles has, to date, focussed solely on Ga self-diffusion at the ^{71}GaAs/^{nat}GaAs interface located approximately at a depth of 0.8 μm. This investigation was done first in order to build a foundation for future analyses of both the Al and the Ga diffusion across heterojunctions. Once the Ga behavior in GaAs is quantitatively known, the individual contributions of Al and Ga diffusion to interfacial disordering can be more easily separated. This serial approach is needed since there is little prior information about Al self-diffusion. Furthermore the monoisotopic character of Al makes it impossible to measure Al self-diffusion using isotopically enriched heterostructures. The contribution of this author to the diffusion modeling was the determination of the net-dopant concentration in the AlGaAs:Si samples. These measurements are an important part of determining the dominant Ga vacancy charge states and energy levels. Of specific interest for the analysis of the Ga self-diffusion dependence on n-type doping is the net-dopant concentration (assumed to be equal to the free carrier concentration) between depths of ~0.5-0.9μm.

5.1.1. ECV Profiles

It is evident in figures 4-3-4-12, that in all annealed samples the net-dopant concentration as measured by the ECV is less than the concentration of Si measured by SIMS. It is possible that compensating impurities were introduced during annealing but

SIMS measurements of p-type impurities such as C and Be showed no such contamination was present at a significant level.

Our general supposition for the whole analysis is that the number of ionized impurities is frozen in during quenching of the sample and thus the net-dopant concentration measured by ECV is nearly identical to the free carrier concentration in the sample immediately prior to quenching. Originally it was believed that the ECV profiles could be accurate enough to input the net-dopant concentration as a function of depth into the diffusion modeling. However, due to the small size of the samples only one attempt at ECV profiling was usually possible, and this limited the ability to assess the accuracy of any one given profile. Since after annealing the Si concentration at the ^{71}GaAs/^{nat}GaAs interface is generally constant and the ECV measurements are assumed to be indicative of the free carrier concentration, only the average net-dopant concentration near the interface was used as input for *n*. While all samples were grown with a nominal Si doping of $5x10^{18}$ cm^{-3}, the annealed samples showed a net-dopant concentration of $1\text{-}3x10^{18}$ cm^{-3}.

This disparity suggests a saturation in the ionized Si concentration and the possible change over of the Si from Ga to As lattice positions. It is also possible, though unverifiable, that the reduced free carrier concentration is caused by the introduction of compensating defects during the annealing or quenching.

5.1.2. Possible ECV Errors

A number of the ECVplots exhibit a significant drop in carrier concentration well before the interface of interest. These profiles deviate significantly from the SIMS

profiles and were not used for the analysis of the Si enhanced self-diffusion. There are a couple of possible causes for these profile shapes, mostly related to non-ideal ECV conditions. The first possibility, and the one we deem most likely, is that during the etching process some oxidation of the aluminum took place creating an insulating film on the surface that distorted the capacitance measurements. Support of this hypothesis comes from experimental observation and known ECV problems. Many samples, though not all, which had an early decline in carrier concentration also had an etched crater which, appeared hazy gray or white in color after removal from the ECV. This is contrast to the majority of samples in which the floor of the etch crater remained nearly specular after ECV profiling. It is noted in the ECV manual that etching difficulty increases with higher Al concentration in AlGaAs and other sources have also reported a difficulties in producing accurate profiles with higher Al concentration (Blood 1985). Finally, with the exception of profile 2b-2 this behavior occurred most often in the samples containing pure AlAs.

Another experimental problem that could cause such profiles is a gradual degradation of the electrolyte. A reduction of ion concentration in the electrolyte would cause the thickness of the depletion region in the electrolyte to become significant (i.e., degradation or loss of Schottky diode condition). The formation of bubbles or deposition of impurities at the sample-electrolyte interface could also reduce the effective area over which the capacitance is measured and thereby reduce the calculated net-dopant concentration. While both of these problems were observed during the measurement of GaAs test samples, there is no reason why they should be more prevalent in samples with higher Al concentrations. Unfortunately the small sample size originally implemented to

conserve the limited amount of material available, prevented duplicate measurements on all but a couple samples under different ECV conditions.

5.1.3. Implications of ECV Measurements

All measured diffusion coefficients were compared to the Ga self-diffusion under intrinsic conditions as measured by the same technique (Bracht, et al. 1998). Using the ratio of diffusion under intrinsic conditions to extrinsic conditions and considering three possible charge states of the Ga vacancy we write

$$\frac{D_{Ga}(n)}{D_{Ga}(n_i)} = \frac{1+\sum_{j=1}^{3}\left(\frac{n}{n_i}\right)^j \exp\frac{jE_f^i - \sum_{j=1}^{3} E_{V_{Ga}^{j}}}{kT}}{1+\sum_{j=1}^{3}\exp\frac{jE_f^i - \sum_{j=1}^{3} E_{V_{Ga}^{j}}}{kT}} \qquad (5.1),$$

Using the net free dopant concentration at the ^{71}GaAs/^{nat}GaAs interface for n, and the values of Blakemore (Blakemore 1982) for E_f^i and n_i, Dr. Bracht used equation 5.1 to find the best fits for the energy levels of the three possible vacancy valences.

If all three vacancy valences are considered, the best fit to all profiles for the various vacancy energy levels given in Table 5.1 suggests the V^{3-} does not contribute to the Ga self-diffusion. If the triply negative vacancy is excluded the fit improves and the error in the energy levels of the other two vacancy species is reduced.

Table 5-1: Vacancy energy level above the valence band for best fits to GaAs:Si data

Species	Energy level (eV) (fit using V^-, V^{2-} and V^{3-})	Energy level (eV) (fit using V^- and V^{2-} only)
V^-	0.38±0.11	0.42±0.04
V^{2-}	0.72±0.19	0.60±0.04
V^{3-}	1.33±4.33	-

The measured Ga diffusion coefficients from all Si and Be doped samples relative to n/n_i are plotted in Figure 5-1 along with the curves predicted from equation 5.1 using the fit considering the presence of V^- and V^{2-} only. For comparison, the dashed line shows the predicted diffusion coefficients using the V^{3-} energy level predicted by Baraff and M. Schlüter (Baraff and Schlüter 1985) and T=872°C.

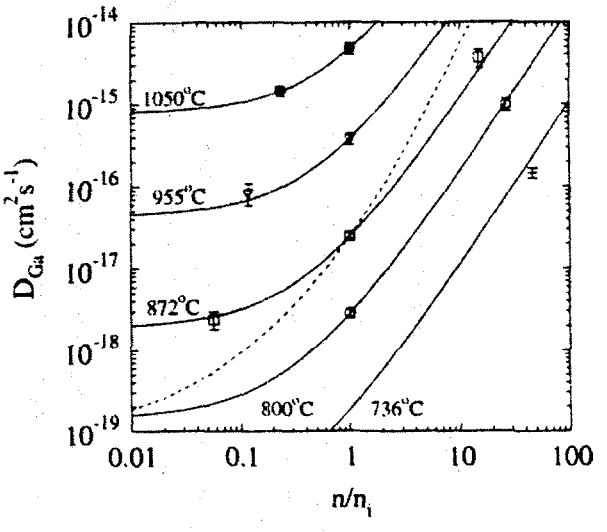

Figure 5-1: Ga self-diffusion coefficient as a function of doping for all Si and Be doped GaAs samples (Bracht, et al. 1999). Solid lines show predicted values using table 5.1 and equation 5.1. The dashed line shows the predicted dependence if the energy levels calculated by Baraff and M. Schlüter are used at T=872°C

5.2. Impurity Enhanced Layer Disordering in GaAs Isotope Superlattices

5.2.1. Zn Profiles

From the simulations it is apparent that the simulated Zn in diffusion profiles do not fit the actual profiles for the complete lengths of the profiles. The upper plateau and the down turn in concentration at the edge of the diffusion front are simulated quite well while the lower concentration Zn tail does not follow the simulation. Such diffusion profiles were shown in published reports (Reichert, et al. 1995) but exact analytic descriptions of such profiles have been enigmatic. Bösker, et al. (1995) described similar profile shapes by overlaying the calculated effects of both I_{Ga}^{3+} and I_{Ga}^{2+} limited reactions. This added reaction

$$I_{Ga}^{2+} + h^{+} \leftrightarrow I_{Ga}^{3+} \qquad (5.2),$$

increases the computational difficulty and was not initially considered in the diffusion simulations. However, the broad, low concentration tail seen in some of our profiles is not present in Bösker et al.'s profiles.

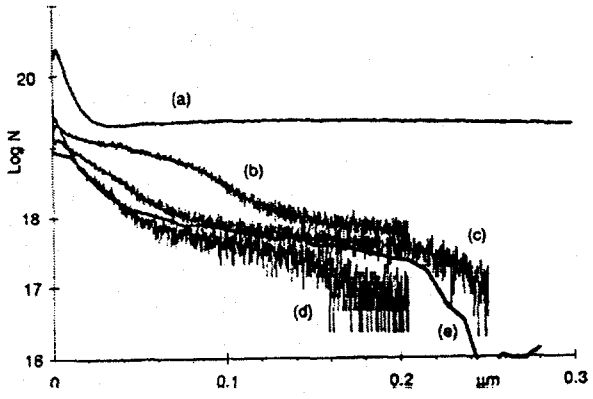

Figure 5-2 GaAs:Zn experiments with surface concentrations similar to those present in our experiments showing a similar broad tail in Zn diffusion profile (Reichert, et al. 1995)

The possibility that a dissociative mechanism [5.3] accompanied the kick-out mechanism was also considered. Prior to adoption of the kick-out model this mechanism had been considered to be the dominant diffusion mechanism for Zn in GaAs (Longini 1962) and was considered here since the onset of the low concentration plateau level appears near the level of the vacancies that should be present in such samples. However, addition of the dissociative reaction did not reproduce the long profile tail.

$$Zn_i + V_{Ga} \Leftrightarrow Zn_s \tag{5.3}$$

The GaAs:Zn ECV measurements matched the general shape of the SIMS profiles and are repeatable using the larger GaAs substrate sample. The ECV results were used for the equilibrium concentration of Zn_s and the close correlation with the SIMS measurements suggests there was not any significant contamination of the samples by electrically active impurities. In this case the ECV concentration results are expected to be more accurate than the SIMS measurements since the SIMS sputter rate had to be quite high (>10Å/sec) to accurately measure the Zn profiles where the lowest detectable concentrations sometimes occurred at depths in excess of 2μm. However, the SIMS results were used to determine the shape of the diffusion profile to eliminate any possible measurements artifacts caused by the increasing error in the ECV profile as the net-dopant concentration decreased.

5.2.2. Disordering Mechanisms

Even though the simulations do not follow accurately the entirety of the SIMS profiles, the Zn diffusion simulation still provides useful information about the superlattice disordering. As noted previously disordering does not progress noticeably

until the Zn concentration exceeds 10^{19} cm^{-3}. This is true for the basic reason that the interstitial concentration is less than 0.1% of the total number Ga lattice sites and thus does not provide enough diffusion flux to enhance the disordering significantly. Since in the high concentration region the simulation fits quite well the actual profile, the disordering by Ga interstitials from kick-out reactions should be accurately described by the included simulations.

Based on these results it is apparent that the disordering is caused by an increase in the equilibrium concentration of gallium self-interstitials, i.e., the Fermi level effect rather than a supersaturation of Ga interstitials. This determination is evident in the GaAs:Zn plots where the calculated I_{Ga} concentration has been included. These plots show that the disordering is correlated to the depth of the Zn diffusion. If supersaturation were the primary mechanism of disordering, the disordering would instead begin ahead of the Zn diffusion front and decrease in I_{Ga} concentration.

The normalized Zn_s and I_{Ga} diffusivities obtained by our fittings fall within the range of values reported in the literature (Bösker, et al. 1999; Yu, et al. 1991). Our values for the Zn diffusivity are more in line with Bösker et al.'s calculation. Our values for the Ga diffusivity agree more closely with Yu's calculations especially if only the higher Zn surface concentration profiles (i.e. those using the 20% alloy source), which give the single largest diffusivity at each temperature, are considered.

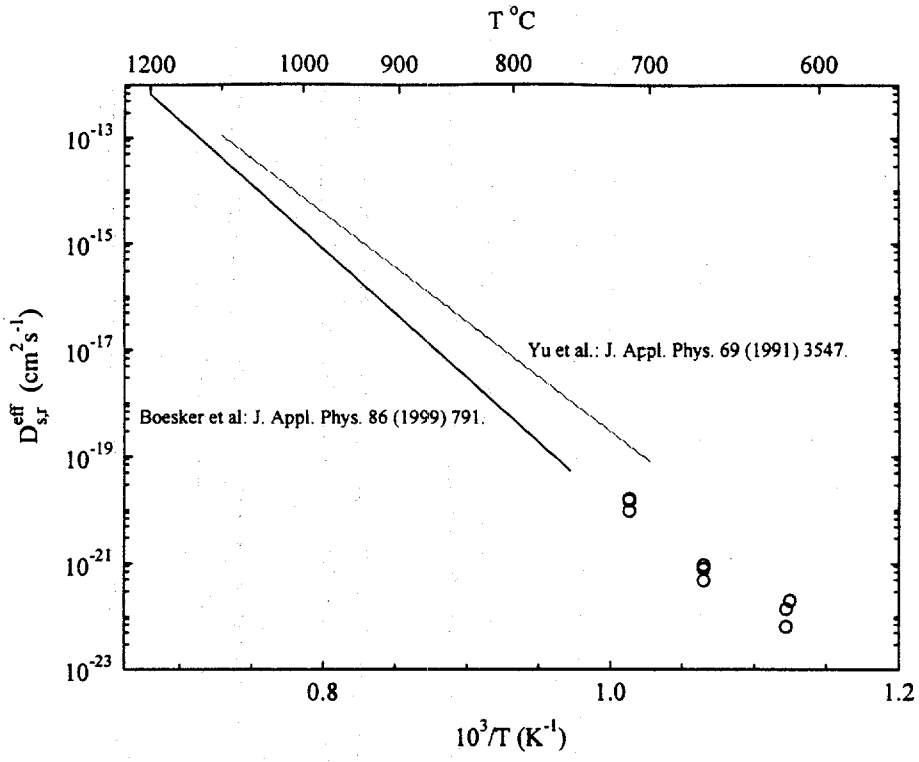

Figure 5-3: Our calculated effective diffusivity of Zn (circles) compared to literature results

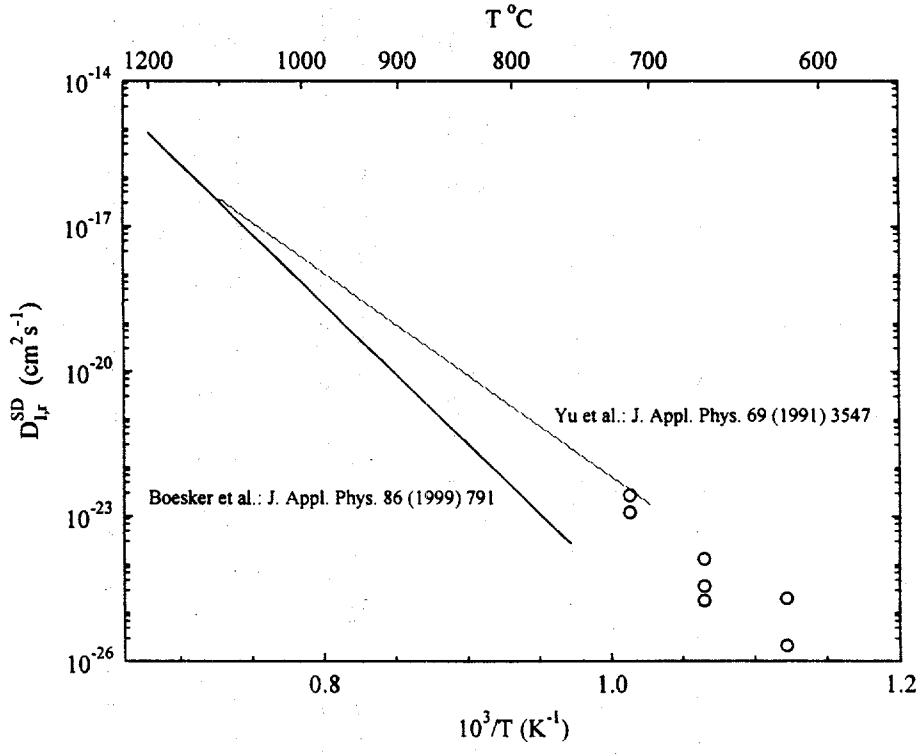

Figure 5-4: Our calculated effective diffusivity of I_{Ga} (circles) compared to literature results

We were not able to make an accurate measurement of the correlation factor. Theoretically, by obtaining values D_I from both the uncorrelated Zn diffusion and the correlated Ga self-diffusion a direct and accurate measurement of the correlation factor should be possible. However, the values we obtained varied between 0.3-1.5 compared to the generally assumed value of 0.5.

6. References.

O. Ambacher, F. Freudenberg, R. Dimitrov, H. Angerer, et al. Japanese Journal of Applied Physics **37**, 2416 (1998)

T. Ambridge and M. M Faktor, Journal of Applied Electrochemistry **4**, 319 (1975).

J. R. Arthur, Journal of Physcial Chemistry of Solids **28**, 2257 (1967).

G. A. Baraff and M. Schlüter, Phys. Rev. Lett. **55**, 1327 (1985).

J.S. Blakemore, J. Appl. Phys. **53**, R123 (1982).

P. Blood, Semiconductor Science and Technology **1**, 7 (1986).

S.E. Blum, M. B. Small and D. Gupta, Appl. Phys. Lett. **42**, 108 (1983).

B. Boltaks, T. D. Dzhafarov, Yu. P. Demakov, and I. E. Maronchuk, Sov. Phys. Semicond. **9**, 545 (1975).

G. Bösker, N. A. Stolwijk, H. G. Hettwer, A. Rucki, W. Jäger, and U. Soervall, Physical Rev. B **52**, 11927 (1995).

J. C. Bourgin, H. J. von Bardeleben, and D. Stievenard, J. Appl. Phys. **64**, R65 (1988).

H. Bracht, E. E. Haller, K. Eberl, M. Cardona, and R.Clark-Phelps, Mat Res. Soc. Symp. Vol **527**, 335 (1998).

H. Bracht, W. Walukiewicz, and E. E. Haller, Mat. Res. Soc. Proc. Vol. **490**, 93 (1998).

H. Bracht, M. Norseng, E.E. Haller, K. Ebert, and M. Cardona, Sol. State Comm. **112**, 301 (1999).

C.R. Brundle, C. A. Evans, Jr., S. Wilson, *Encyclopedia of Materials Characterization* (Butterworth-Heineman, Stoneham, MA, 1992).

H.C. Casey Jr. and M. B. Panish, Transactions of the Metallurgical Society of AIME **242**, 406 (1968).

M.P. Chase, M. D. Deal, and J. D. Plummer, J. Appl. Phys **81**, 1670 (1997).

C.-H. Chen, U.M. Gösele and T.Y. Tan, Applied Physics A **68**, 9 (1999).

R.M. Cohen, Materials Science and Engineering **R20**, 167 (1997).

J. Crank. *The Mathematics of Diffusion.* (Clarendon Press, Oxford, 1975).

L. S. Darken, Transactions of the American Institute of Mineral and Metallurgical Engineers **175**, 184 (1984).

D.G. Deppe and N. Holonyak, Jr., J. Appl. Phys **64**, R93 (1988).

F. H. Eisen and C. E. Birchenall, Acta Met. **5**, 265 (1957).

H. D. Fuchs, W. Walukiewicz, E. E. Haller, W. Dondl, R. Schorer, G. Abstreiter, A. I. Rudnev, A. V. Tikhomirov, and V. I. Ozhogin, Phys. Rev. B **51**, 817 (1995).

Y. Gao, J. Appl. Phys. **64**, 3760 (1988).

S.K. Ghandi. *VLSI Fabrication Principles: Silicon and Gallium Arsenide* (John Wiley and Sons, N.Y., 1994).

U. Gösele, F. Morehead, J. Appl. Phys. **52**, 4617 (1981).

E.E. Haller, MSE 223 Class Notes, University of California (Fall 1997).

E.E. Haller, J. Appl. Phys. (Reviews) **77**, 2857 (1995).

J. C. Hu, M. D. Deal and J. D. Plummer, J. Appl. Phys. **78**, 1595 (1995).

T. Humer-Hager, R. Treichler, P. Wurzinger, H. Tews and P. Zwicknagl, J. Appl. Phys **66**, 181 (1989).

W. Jäger, A. Rucki, K. Urban, H.-G. Hettwer, N. A. Stolwijk, H. Mehrer, and T. Y. Tan, J. Appl. Phys. **74**, 4409 (1993).

A. S. Jordan, Journal of the Electrochemical Society: Solid State Science **118**, 781 (1971).

D.L. Kendall, A. M. Bartning, Boletin del Instituto Tonantzintla **2**, 257 (1977)

N. H. Ky, J. D. Ganiere, F. K. Reinhart and B. Blanchard, J. Appl. Phys. **79**, 4009 (1996).

W.D. Laidig, N. Holonyak, Jr., M. D. Camras, K. Hess, J. J. Coleman, P. D. Dapkus, and J. Bardeen, Appl. Phys. Lett. **38**, 776 (1981).

J. W. Lee and W. D. Laidig, Journal of Electronic Materials **13**, 147 (1984).

R. L. Longini, Solid State Electronics **5**, 127 (1962).

R. L. Longini and R. F. Greene, Physical Review **102**, 992 (1956).

M. Luysberg, W. Jäger, K. Urban, M. Schänzer, N. A. Stolwijk, H. Mehrer, Material Science Engineering B **13**, 137 (1992).

J. R. Manning, Physics Review **124**, 470 (1961).

MellWood Laboratories, Inc. (West Lafeyette, IN).

B. L. Olmsted and S. N. Houde-Walter, Appl. Phys. Lett. **60**, 368 (1992).

B. L. Olmsted and S. N. Houde-Walter, Appl. Phys. Lett. **63**, 530 (1993).

H. D. Palfrey, M. Brown and A.F. Willoughby, Journal of the Electrochemical Society **128**, 2224 (1981).

W. Reichert, C. Y. Chen, W. M. Li, J. E. Shield and R. M. Cohen, J. Appl. Phys. **77**,1902 (1995).

K.K. Shih, Journal of the Electrochemical Society: Solid-State Science and Technology **123**, 1737 (1976).

T. Urisa and K. Kajiyama, Japan. J. Appl. Phys. **15**, 1607 (1976).

L. Wang, J. A. Wolk, L. Hsu, E. E. Haller, J. W. Erickson, M. Cardona, T. Ruf, J. P. Silveira, and F. Briones, Appl. Phys. Lett., **70**, 1831 (1997).

L. Wang, L. Hsu, E. E. Haller, J. W. Erickson, A. Fischer, K. Eberl, and M. Cardona, Phys. Rev. Lett., **76**, 2342 (1996).

D. Weiler and H. Mehrer, Philosophical Magazine A, **49**, 309 (1984).

R. G. Wilson, Solid State Electronics **39**, 1113 (1996).

W. Yang, A. Gopinath and M. Hibbs-Brenner, IEEE Photonics Technology Letters **7**, 848 (1995).

S. Yu, T. Y. Tan, and U. Gösele, J. Appl. Phys. **69**, 3547 (1991).

S. Yu, T. Y. Tan, and U. Gösele, J. Appl. Phys. **70**, 4827 (1991).

H. Zimmerman, U. Gösele, and T. Y. Tan, J. Appl. Phys. **73**, 150 (1993).

7. Appendix

7.1. Characterization Techniques

7.1.1. SIMS

Secondary ions mass spectroscopy (SIMS) is an extremely powerful tool for precisely determining the chemical composition of a material. SIMS is most commonly used to determine the chemical composition as a function of depth (Dynamic SIMS, usually referred to simply as SIMS) but can also be used to image the chemical composition of a given surface (Static SIMS). Dynamic SIMS is the specific mode of operation that will be discussed here. By using a well controlled ion beam to slowly sputter away the surface of a material and then collecting back-scattered ions of a given charge to mass ratio, SIMS can detect atomic concentrations down to 10^{13}-10^{16} atoms/cm^3 with depth resolutions of 50nm or less (Wilson 1996).

7.1.1.1. Sputtering

Typically O^+, Ar^+, Ga^+ or Cs^+ ion beams with energies in the 1-10 keV range are used to sputter away the sample. The energetic ions penetrate into the sample and create a mixing zone where energy is transferred to atoms in the sample, some of which are hence ejected from the surface of the mixing zone. The thickness of this mixing zone sets the fundamental limit of SIMS depth resolution. The depth of the mixing zone depends on the ion energy, impinging species, and matrix material but is generally around 2-50nm. For a given energy and geometry heavier ions such Cs^+ create a smaller zone and thus give the best depth resolution. Since the ion energies affect the sputter rate and since there is a distribution of energies across the width of the ion beam, the beam is rastered

across a small square area to produce a uniform flux of ions to sample. This constant ion flux produces a crater with a bottom that ideally is perfectly parallel with the original sample surface. In practice, any surface will roughen with increased sputtering time and transpose surface texture into crater roughness. This along with possible sample misalignments determines the actual depth resolution of SIMS which decreases with depth.

For accurate depth profiling the ion flux to the sample should be kept constant to maintain a constant sputter rate. After the sputtering is complete the crater depth is measured by a profilometer or other means to convert sputter time into depth. However, the sputter rate will vary with changes in the matrix composition so the sputter rates of disparate materials must be corrected for to obtain accurate depth profile of heterostructures.

7.1.1.2. Detection

Ejected ions are collected by a mass spectrometer that separates ions for detection based different mass/charge ratios. A typical mass spectrometer can collect only positive or negative charged particles so the sensitivity to individual species depends on their ion yield and the polarity of the ion detector. In order to obtain the most accurate depth profiles the collected ions need to originate at the center of the sputtered crater since ions from the edge may include secondary ions that have been sputtered from the sidewalls of the crater or other edge effects. Using apertures ions can be collected from the center 50 μm^2 of a 250 μm^2 crater.

Often the most easily formed ion of the most prevalent isotope of a given species is collected in order to obtain the largest spectrometer signal. However, other isotopes can be collected along with beam-sample conjugates such as $CsBe^+$ to limit mass interference or CsM^+ to limit matrix effects (Gao 1988). Correlating a given amount of collected ions to the actual species concentration in the sample requires "standard" samples. Because the ion yield of a species depends on its chemical environment and specific beam conditions the standard matrix should be identical to the sample and the standard profile should be recorded soon before or after taking the sample profile.

7.1.1.3. Profile Artifacts

Even after correcting for the sputter rates in the various materials and calibrating the species concentrations with measurement of standards there are artifacts of the measurement technique which slightly distort the actual concentration vs. depth profile.

The first artifact to be discussed is the so-called "knock on" effect. While the ion-sample energy transfer causes some atoms to be sputtered back towards the beam, some atoms are displaced further into the sample. Hence, while SIMS can give a very accurate depth profiles of samples with constant atomic concentrations, concentration gradients appear distorted to a degree that depends on the size and direction on the gradient. Knock-on effects are most apparent at abrupt junctures of a given species going from high to low concentrations, since while the number of atoms pushed deeper into the sample may remain nearly constant. The increase in concentration due to knock-on can dominate the total collected signal when the crater reaches the low side of the junction. Conversely, at abrupt low-high junctions knock-on has a minimal effect, since the

concentration increase from knock on is zero or so small as to often be below the sensitivity of the instrument. Knock on effects are harder to explicitly identify at junctions displaying intermediate concentration gradients.

Instrumental broadening (a experimental uncertainty present in all SIMS measurements) and surface effects also may create artifacts in the final data. Instrumental broadening occurs because the sample is continuously sputtered during the finite (~0.1-1 sec) secondary ion collection time, so an ion count at a given time/depth is actually the average of a small range of depths and represents an average depth slightly deeper than the ion species collected immediately prior. If an as grown heterostructure is assumed to have abrupt interfaces, instrumental broadening can be corrected for by using a deconvolution function. Surface oxidation or other contaminants change the chemical environment at the surface that will effect the ion yield of the various species. Oxidation specifically will increase the yield of positive ions making the initial few data points unusable.

7.1.2. ECV

An accurate knowledge of the net dopant concentration as a function of depth is essential to the characterization of modern semiconductor material structures for devices and dopant diffusion studies. Both spreading resistance and conventional C-V techniques have been used traditionally to perform the necessary measurements but both have limitations. Spreading resistance measurements require a skilled operator, a large amount of time for precision lapping to prepare the structures and for reducing the complex raw data to obtain accurate results. While conventional C-V measurements are straight

forward, the depth is limited by the reverse break down voltage of the diode. For highly doped structures this limits conventional C-V measurements to the extreme near surface region of structures (<100 Å for 10^{18} cm^{-3} doped GaAs).

Electrochemical Capacitance Voltage (ECV) measurements offer the benefit of profiling net dopant concentration to almost unlimited depths and relatively simple operation. First described in 1975 (Ambridge and Faktor, 1975), the technique uses an electrolyte in contact with the semiconductor surface to form both a Schottky barrier for C-V measurements under reverse bias and a medium for etching progressively deeper into the semiconductor structure under forward biasing of the sample. A schematic of the cell used for such measurements appears in Figure 9-1.

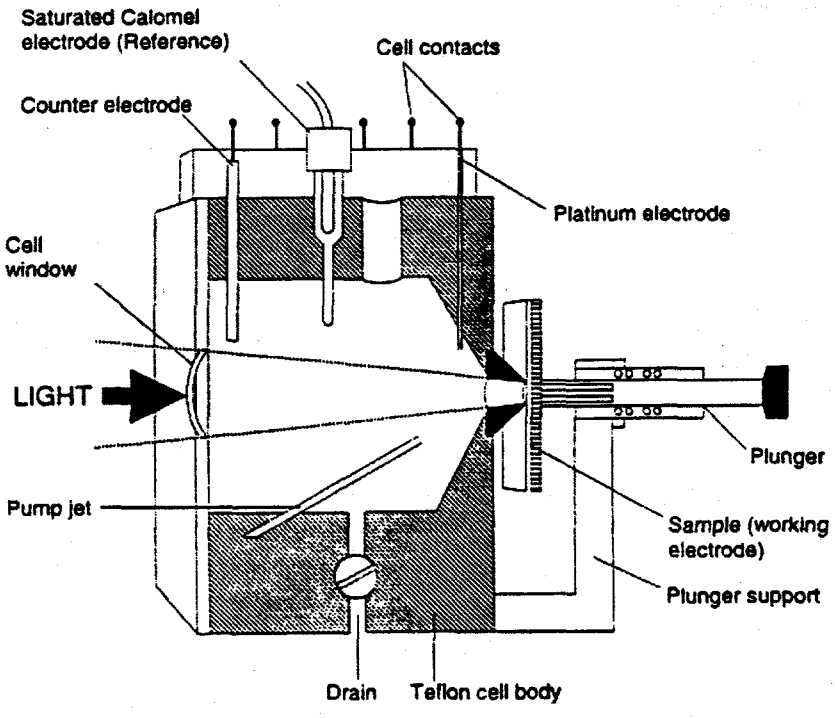

Figure 7-1: ECV Cell

In addition for the reservoir of electrolyte and the sample the other critical components of the apparatus are the sealing ring which defines the area of contact between the electrolyte and sample, the counter electrode which measures the current during etching, the reference electrode for calibration of the voltage signals and the light source for generating minority carriers (holes) during the etching of n-type samples.

7.1.2.1. Measuring Net Dopant Concentration

A Schottky diode is formed if the ion concentration in the electrolyte is much greater than the carrier concentration in the semiconductor. Under reverse bias condition the depletion region is essentially confined completely to the semiconductor. The depletion depth, W_d, and capacitance of the depletion region, C, are given by the equations:

$$W_d = \left[\frac{2(\Phi - V)\varepsilon_o \varepsilon_r}{qN}\right]^{\frac{1}{2}} \tag{7.1}$$

$$C = A\left[\frac{qN\varepsilon_o \varepsilon_r}{2(\Phi - V)}\right]^{\frac{1}{2}} \tag{7.2}$$

While N in the preceding equations is the total space charge (ionized net dopant concentration) in the depletion region corresponds to the free carrier concentration at the depletion edge. Using the differential capacitance vs. voltage characteristics this local net dopant concentration is given by:

$$N = \frac{1}{q\varepsilon_o \varepsilon_r A^2} \bullet \frac{C^3}{dC/dV} \tag{7.3}$$

The capacitance and differential C/V parameters in this equation are measured using a modulated high frequency (0.5-30 kHz) voltage.

7.1.2.2. Etching

The essential advantage of the ECV technique is the ability to slowly and uniformly dissolve the semiconductor perpendicularly to the plane of the original surface. In an optimized electrochemical system the charge transfer from the semiconductor to the electrolyte is balanced by the creation of holes in the valence band of the semiconductor. These holes facilitate dissolution of the semiconductor by reactions such as that the one given in equation 7.4.

$$GaAs + 6h^{+} \Leftrightarrow Ga^{3+} + As^{3+} \tag{7.4}$$

Since by definition there is a large population of holes in p-type materials, applying a forward bias to the semiconductor/electrolyte junction will allow the dissolution of the semiconductor. In n-type materials hole populations must be created which is done by illuminating the sample with light that has energy greater than the semiconductor band gap.

By measuring the charge transfer between the working electrode (i.e. the sample) and the counter electrode in the electrolyte the amount of material which has been etched away can be calculated using Faraday's equation:

$$W_r = \frac{M}{zF\rho A}\int_0^t Idt \tag{7.5}$$

The total depth at which incremental capacitance measurements take place are then given simply by:

$$Depth = W_r + W_d \tag{7.6}$$

7.1.2.3. Other Considerations

The local carrier concentration measurements and depth calculations above assume an abrupt edge to the depletion region. This is not strictly true; carriers will diffuse some finite distance past the depletion edge. The average diffusion distance is given by the Debye length, L_d and limits the depth resolution of the ECV to approximately three times the Debye length (Blood). Table 7-2 shows the depth resolution dependence on the carrier concentration in the material.

$$L_d = \frac{1}{q}\left[\frac{\varepsilon_o \varepsilon_r KT}{N}\right]^{\frac{1}{2}} \tag{7.7}$$

Table 7-2

Log N (in cm^{-3})	Debye Length, L_d (μm)	Resolution (μm)
20	0.0004	0.0013
18	0.004	0.013
16	0.04	0.13
14	0.4	1.3